Aspects of fault zones around the Rotliegend reservoirs and the possible effects of salt in the fault zones on rates of seismicity in these zones

Report of a short project in April - May 2016

Janos L. Urai (1), Michael Kettermann (1), Streffen Abe (2), Simon Virgo (1)

(1)
Structural Geology, Tectonics and Geomechanics
RWTH Aachen University, Lochnerstrasse 4-20
D-52056 Aachen, Germany
www.ged.rwth-aachen.de

(2)
Institut für geothermisches Ressourcenmanagement
Berlinstr. 107a
D-55411 Bingen
www.igem-energie.de

Supervision:
ir J.P.A.Roest, State Supervision of Mines, Ministerie van Economische Zaken,
Henri Faasdreef 312 | 2492 JP | Den Haag

igem Institut für geothermisches Ressourcenmanagement
EMR Energy & Mineral Resources Group | RWTH AACHEN UNIVERSITY

Summary

This study investigates the mechanical effect of salt in dilatant normal faults. During tectonic faulting in the Groningen area, rock salt may have flown downwards into dilatant faults, which thus may contain lenses of rock salt at present. Because of its viscous properties, the presence of salt lenses in a fault may introduce a strain-rate dependency to the faulting and affect on the distribution of magnitudes of seismic events.

Our results are a "proof of concept" and show that the above processes can be investigated using the methods proposed. Full scaling and discussion of the importance of these processes to induced seismicity in Groningen require further, more detailed study.

In the first part of the study we investigate how salt flows into dilatant faults, using analog models. The experiments are based on a simplified stratigraphy of the Groningen area, where it is generally thought that most of the Rotliegend faulting has taken place in the Jurassic, after deposition of the Zechstein. This is interpreted to mean that at the time of faulting the sulphates were brittle anhydrite. If these layers were sufficiently brittle to fault in a dilatant fashion, rock salt could flow downwards into the dilatant fractures. To test this hypothesis, we use sandbox experiments where we combine cohesive powder as analog for brittle anhydrites and carbonates with viscous salt analogs in two experiments to explore the developing fault geometry and the resulting distribution of salt in the faults. Our results are consistent with earlier results discussed in detail in the publications cited.

In the second part of the study we investigate the stick-slip behavior of fault zones containing ductile material, using the Discrete Element Method (DEM). The method has been successfully used previously to model the stick-slip behavior of rough faults. Ductile materials were developed for DEM in previous studies of our group, which makes it possible to study the stick-slip motion of fault models with brittle and ductile components. The aim of the work presented here was to investigate if the method is suitable for the investigation of the loading rate dependence of the seismicity generated by a fault containing salt. Results show that the DEM approach is in principle suitable for the modeling of the seismicity of faults containing salt: the stick-slip motion of the fault becomes dependent on shear loading rate with a modification of the frequency magnitude distribution of the generated seismic events. However, large parts of the parameter space of fault geometry, salt rheology and loading rate remain unexplored, so that the development of models which can be applied to induced seismicity in the Groningen field requires more work.

The main conclusions of this study are:

(1) If the carbonates and anhydrites of the base Zechstein formed dilatant faults, the overlying rock salt could have flown into the open fractures, forming fault zones with salt lenses
(2) The distribution of salt in the fault zone a fault zone is controlled by the failure mode of the underlying rocks, the fault geometry, the rate of faulting and the rheology of the overlying salt.
(3) DEM can model seismicity of faults containing salt
(4) Salt makes fault behavior dependent on shear loading rate
(5) This results in a complex interplay between stick-slip dynamics of fault and visco-elastic behavior of salt

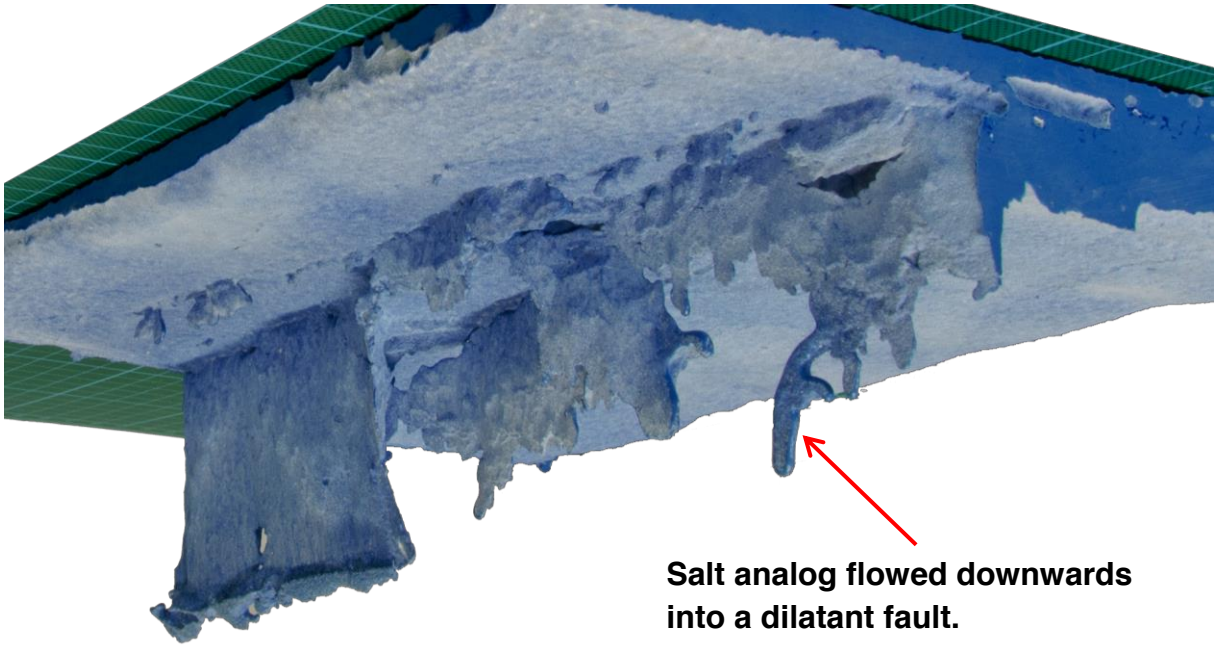

Salt analog flowed downwards into a dilatant fault.

Dilatant fault zone that formed underneath a salt analog.

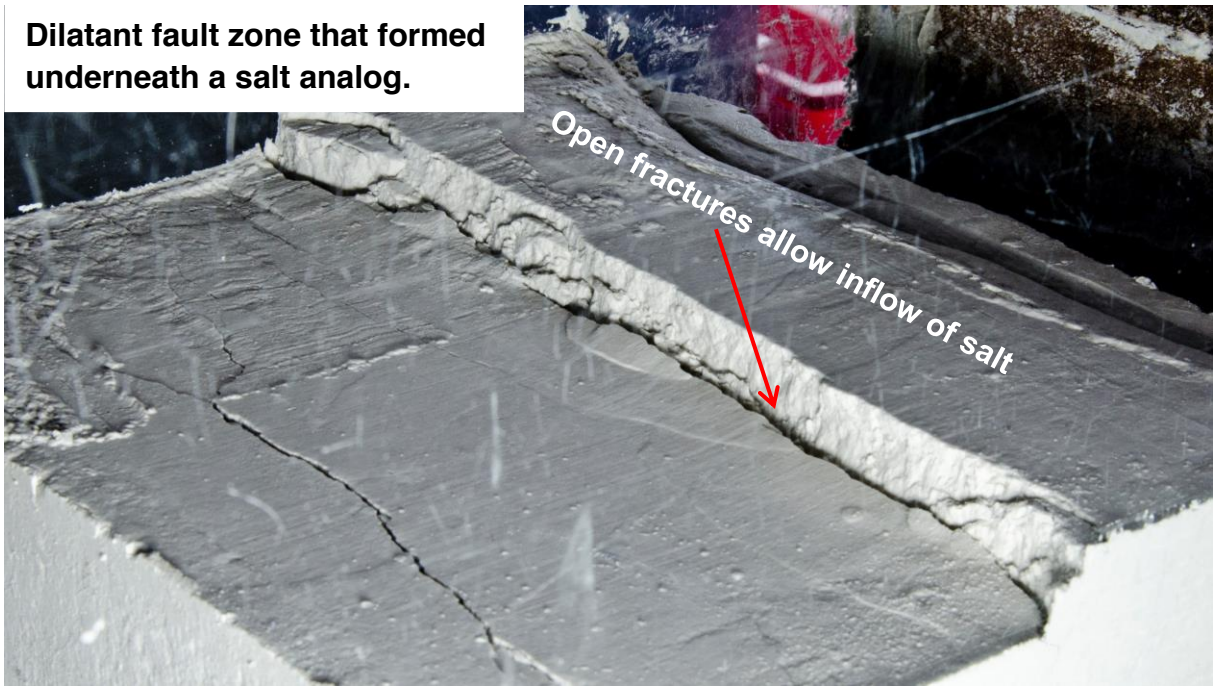

Setup of a discrete element method simulation

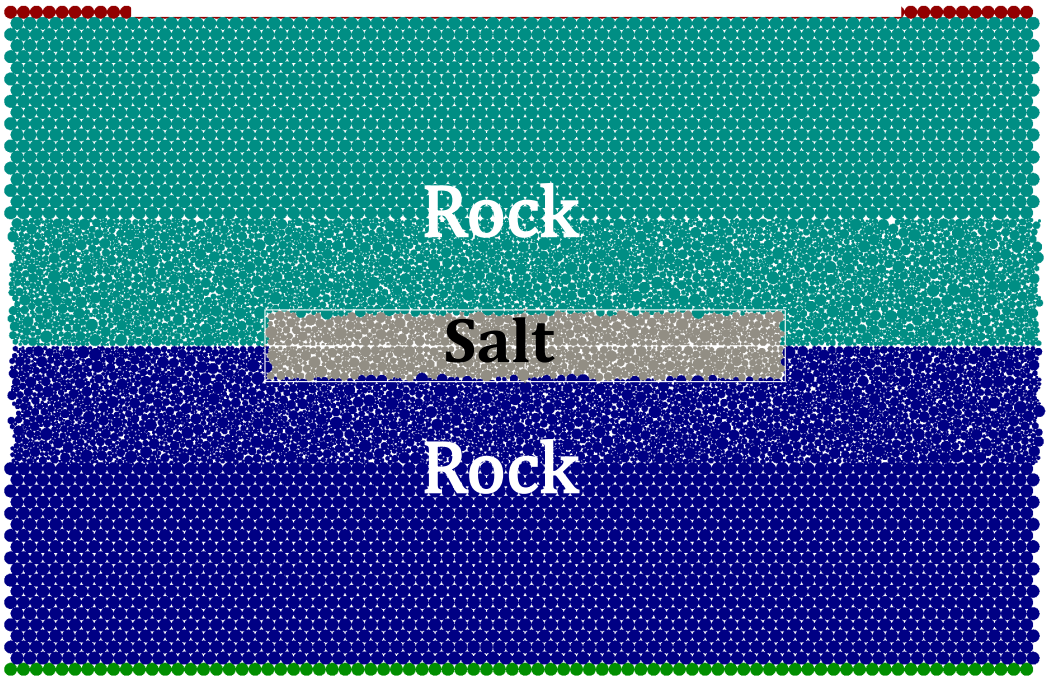

Results of the DEM models show fewer strong events at higher movement velocities

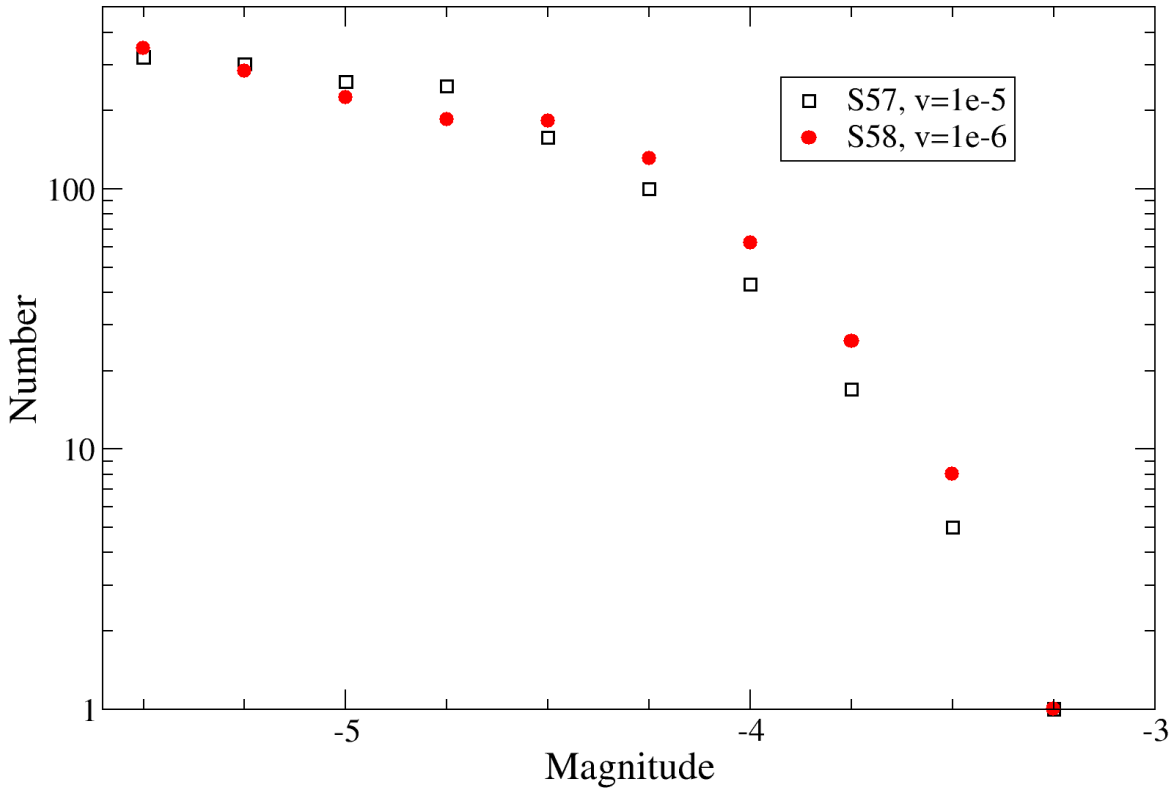

Analogue modelling of salt intrusion into dilatant faults

1. Abstract

This study investigates the lubricating effect of salt in dilatant normal faults. As rock salt can flow in a ductile fashion at low strain-rates and break at high strain-rates, its presence in a fault introduces a strain-rate dependency to the faulting, that in turn can have an effect on the distribution of magnitudes of seismic events. In this part of the study we demonstrate how salt flows into opening dilatant faults using analog models. The experiments shown are based on the stratigraphy of the Groningen area, where the Permian Z1 - Z3 carbonates and anhydrites are overlain by the Z3 & 4 salts before faulting.
It is generally thought that most of the Rotliegend faulting has taken place in the Jurassic, after deposition of the Zechstein, related to the break-up and progressive rifting of the Pangea supercontinent. This was followed by reactivation and inversion during the Late Cretaceous and Early Cenozoic, related to the Alpine orogeny, but this has affected the Groningen area only slightly. This means that at the time of faulting there was sufficient overburden on the Z1 - Z3 to ensure that the sulphates were brittle anhydrite. We propose that these layers were also sufficiently brittle to fault in a dilatant fashion, allowing the rock salt to flow downwards into the dilatant fractures. To test this hypothesis, we combine cohesive powder as analog for brittle carbonates with viscous salt analogs in two experiments and show both the developing fault geometry and the resulting geometry of salt in the faults.

These experiments are seen as "proof of concept", while full scaling and discussion of all processes which may transport salt into a dilatant fault require further, more detailed study.

2. Introduction

Faulting (under drained conditions) in brittle rocks is to first order a strain-rate independent process. That means a fault will develop in similar fashion independent of the rate of the underlying driving process. Rock salt however behaves different: it can flow at slow strain-rates and break at high strain-rates. Hence, introducing salt into a fault zone adds a rate-dependency to the faulting process. In case such a fault is a potential hypocenter for induced seismic events one may expect that the distribution of magnitudes can change with the overall movement rate. This effect has yet to be investigated in detail.
Investigating the problem at hand requires a twofold approach. First it has to be shown, that dilatant faults can form beneath a viscous salt layer and that the salt then flows into the developing space. Secondly the effect of the salt in the faults on earthquake magnitudes has to be investigated. The first step shown here is done

using analog modeling, while for the second step a discrete element numerical model was used.

Analog modelling of dilatant faulting is usually done using cohesive powders (e.g. Holland et al., 2006, 2011; Galland et al., 2009; van Gent et al., 2010; Abdelmalak et al., 2012). We use hemihydrate powder as its properties have been studied in great detail and its suitability has been shown (Figs.1-3, van Gent et al., 2010; Holland et al., 2011). Moreover, the material can be wetted after deformation and thus harden, which allows for excavation and preservation of the faulted material (Kettermann and Urai, 2015).

Combinations of fluids and cohesive powders have been used to model magma emplacement (Galland et al., 2006, 2007, 2009; Abdelmalak et al., 2012), however in these models a low viscosity fluid is pumped beneath the cohesive layer, forming open fractures at the free surface of the powder.

In the presented models the powder layer is covered by a high viscosity fluid. Kettermann and Urai (2015) have shown that dilatant faults can form in cohesive materials even when they are buried. This requires a small vertical stress (maximum principal stress), i.e. thin overburden thickness, so that the least principal stress can become negative when it intersects the Mohr-Coulomb failure criterion (Fig. 4). In our models we can conveniently adjust the failure mode by controlling the thickness of the viscous cover layer.

3. Experiments

The presented experiments are based on the three basic assumptions that (1) the rocks beneath the salt are failing in hybrid or extensional failure with (2) a strain rate slow enough to allow the salt to fill the opening space by (3) viscous salt flow.

The study is intended to look into the behavior of sub-salt faults in the Groningen area, hence we have chosen the models stratigraphy to roughly represent the natural stratigraphy with a length-scaling factor of 1:10 000, meaning 1 cm in the model represents 100 m in nature. Faults in the Permian anhydrites and carbonates beneath the Z3 and Z4 salts are expected to have formed after the deposition of the evaporites. This shallow burial depth means there was not very much overburden pressure and hence we can assume a hybrid or extensional faulting in the carbonates and anhydrites (see introduction and Kettermann and Urai, 2015).

To adjust the fault's failure mode, we need to scale the overburden thickness (i.e. the salt analog thickness) not by length but by vertical stress. Using the above introduced 1:10 000 scaling factor would require a salt analog thickness of > 3 cm, however the weight of this layer would push the brittle rock analogs more towards shear failure as the differential stress increases. Hence we use salt analog thicknesses of 1.2 - 2.5 cm in order to scale the failure mode properly (Kettermann and Urai, 2015).

Making use of these assumptions and scaling rules we perform two experiments with different approaches to show two aspects of the dynamic salt-faulting interaction:

(1) We use a hardening resin as salt analog which allows post mortem investigation of the 3D structure of the salt that has entered developing open fractures.
(2) We use a transparent salt analog which allows 3D observations of fault formation underneath a salt layer. Hardening the powder post mortem allows for a detailed investigation of the fault zone itself.

Additionally we vary the basement fault angle from 63° to 70° to cover a range of potential basement fault geometries (precursor or graben domain, Nollet et al., 2012).

3.1. Experiment 1: Hardening resin above cohesive powder

In this experiment we used a resin with a density of approx. 1.7 g/cm³ and an estimated viscosity of 50 Pas as salt analog above layers of hemihydrate powder and sand. The basement fault of the deformation rig was 70° causing a fault development in the precursor domain. Thicknesses of the individual layers are shown in Figure 6. As the resin starts to harden after 30 minutes the maximum displacement of 16 mm was reached in this time. The formation of the fault as well as the salt entering it can be seen on Figure 7.

After hardening the resin, we removed the powder and could then investigate the structure of the 'salt in the fault'. The resin shows a detailed negative of the fault zone (see upside down photograph Fig. 8). It becomes apparent that not only vertical but also lateral salt flow contributes to the distribution of salt within the fault. At several places fragments of the powder were entrained into the resin and leave cavities in it. We provide a high resolution 3D model of this structure (Fig. 9). These observations compare well to those made by Holland et al. (2011) from CT-scans of dilatant fault networks without viscous cover layers.

3.2. Experiment 2: Hardening powder beneath transparent salt analog

In this second experiment we used a transparent, well characterized highly viscous silicone oil as salt analog (Korasilon G30M, density ~ 0.98 g/cm³, viscosity $3*10^4$Pas) allowing for top-view observation of the developing fault in the powder layer. The basement fault angle was set to 63° (graben domain) and the maximum displacement was 15 mm at a deformation velocity of 1.2 mm/h. Post mortem we hardened the powder and could investigate the fault zone in 3D. The detailed setup is shown in Figure 11. Adding the silicone-oil on top of the sensitive powder layer was done by letting it flow over it from one side over a period of 20 h (Fig. 12).

The formation of the faults is shown in Figure 13 in side-view. Hardening the hemihydrate powder after the deformation allowed us to then remove the silicone and study the fault in 3D in detail. As a result of the smaller basement fault angle faults are dipping shallower, but still show strong dilatancy (Figs. 14-17). As the silicone deeply entered the open fractures some volume of it remained inside when removing the layer as it was interlocked with the rough fracture surfaces. However, when turning over the removed silicone oil layer a negative of the fault zone is visible and it is clear that the material entered the opening space of the dilatant faults (Fig. 17).

4. Conclusions

Under the assumptions that the carbonates and anhydrites beneath the Z3 & Z4 salts of the Groningen area form faults in hybrid or dilatant failure, the presented analog models clearly show that:

(1) Salt flows into opening fractures and faults in underlying brittle rocks
(2) Lateral flow of the salt can bring salt into extensional jogs even beneath non-dilating parts of the fault zone
(3) The extent to which salt will flow into a fault zone is strongly controlled by the failure mode of the underlying rocks, the fault domain (i.e. precursor or graben domain) and the overall fault geometry.

5. References

Abdelmalak, M.M., Mourgues, R., Galland, O., Bureau, D., 2012. Fracture mode analysis and related surface deformation during dyke intrusion: Results from 2D experimental modelling. Earth and Planetary Science Letters 359-360, 93–105.

Galland, O., Cobbold, P.R., de Bremond d'Ars, J., Hallot, E., 2007. Rise and emplacement of magma during horizontal shortening of the brittle crust: Insights from experimental modeling. Journal of Geophysical Research 112, B06402.

Galland, O., Cobbold, P.R., Hallot, E., de Bremond d'Ars, J., Delavaud, G., 2006. Use of vegetable oil and silica powder for scale modelling of magmatic intrusion in a deforming brittle crust. Earth and Planetary Science Letters 243, 786–804.

Galland, O., Planke, S., Neumann, E.-R., Malthe-Sørenssen, A., 2009. Experimental modelling of shallow magma emplacement: Application to saucer-shaped intrusions. Earth and Planetary Science Letters 277, 373–383.

Holland, M., Urai, J.L., Martel, S., 2006. The internal structure of fault zones in basaltic sequences. Earth and Planetary Science Letters 248, 301–315.

Holland, M., van Gent, H.W., Bazalgette, L., Yassir, N., Hoogerduijn Strating, E.H., Urai, J.L., 2011. Evolution of dilatant fracture networks in a normal fault — Evidence from 4D model experiments. Earth and Planetary Science Letters 304, 399–406.

Kettermann, M., Urai, J.L., 2015. Changes in structural style of normal faults due to failure mode transition: First results from excavated scale models. Journal of Structural Geology 74, 105–116.

Nollet, S., Kleine Vennekate, G.J., Giese, S., Vrolijk, P., Urai, J.L., Ziegler, M., 2012. Localization patterns in sandbox-scale numerical experiments above a normal fault in basement. Journal of Structural Geology 39, 199–209.

van Gent, H.W., Holland, M., Urai, J.L., Loosveld, R., 2010. Evolution of fault zones in carbonates with mechanical stratigraphy – Insights from scale models using layered cohesive powder. Journal of Structural Geology 32, 1375–1391.

DEM Modelling of the stick-slip dynamics of Faults containing Salt

6. Motivation

One possible approach to the study of the mechanical behaviour of faults containing not only brittle-elastic / frictional, but also ductile, materials is numerical modelling using a Discrete Element Method (DEM) approach. The method has been successfully used previously to model the stick-slip behaviour of rough faults (Weatherley and Abe, 2004; Abe et al., 2006; Fournier and Morgan, 2012). A method to include ductile materials into the DEM models was introduced by Abe and Urai (2012), which makes it possible to study the deformation behaviour of mixed brittle / ductile structures.
The aim of the work presented here was to ascertain if the method is suitable for the investigation of the loading rate dependence of the seismicity generated by a fault containing salt.

7. Method

7.1. The Discrete Element Method

The Discrete Element Method (Cundall and Strack, 1979; Mora and Place, 1994; Place and Mora, 1999; Potyondy and Cundall, 2004) is a numerical modelling approach for the simulation of the mechanics of a wide range of materials. The model consists of spherical particles which are interacting with their nearest neighbours. From these interactions the forces and moments acting on each particle can be calculated and the particle movements are then computed from the interaction forces using Newton's law. The details of the interactions determine the macroscopic mechanical behaviour of the material. Interactions include “bonded” interactions (Fig. 18) which can break irreversibly if a deformation threshold is exceeded (Potyondy and Cundall, 2004, Wang et al., 2006), elastic-frictional contact interactions (Fig. 19) and velocity dependent “dashpot” interactions (Abe and Urai, 2012).
In the present work the microscopic interaction parameters are chosen such that the macroscopic elastic and fracturing behaviour of the model “rock” material closely resembles that of a linear elastic solid. Frictional-elastic interactions are used for the contact interactions along the broken parts of a fault, i.e. the normal force is calculated using a linear elastic contact law and the tangential force is calculated using a Coulomb friction law as described by Cundall and Strack (1979). For the ductile model material a combination of an elastic contact interaction and a “dashpot” interaction has been used in parallel, i.e. at the particle level a Voigt-Kelvin material is simulated. Calibration of this type of model material (Abe and Urai, 2012) has shown that the macroscopic behaviour closely resembles a viscous material with an added

yield stress similar to a Bingham material (Fig. 22). The viscosity of this material can be adjusted within a limited range by modifying the damping parameter *a* in the "dashpot" interaction (Eq. 3 in Abe and Urai, 2012).
In order to enable the simulation of sufficiently large models, an implementation of the DEM for parallel computers, ESyS-Particle, based on the parallelisation approach by Abe et al. (2003), has been used. As an additional measure to reduce the computational cost of the simulations the dimension of the models has been restricted to a 1D fault embedded in a 2D brittle-elastic medium.

7.2. Seismic event statistics

In the numerical models the seismic events are not detected in the "traditional" way by recording propagated waves but instead the released seismic energy is calculated directly from the drop in elastic energy stored in the model during an event (Fig. 23). The approach taken for the calculations is the same which has shown to be successful by Weatherley and Abe (2004). The elastic energy stored in all particle-particle interactions in the model is summed up at every time step considered and tracked over time (red curve in Fig. 23). Time periods where the time derivative of the stored elastic energy is negative, i.e. energy is released, are considered "events". In order to avoid the detection of too many spurious events due to numerical noise in the models the energy curve is smoothed using a "leaky integrator" scheme (Weatherley and Abe, 2004). After the events have been detected the difference between the stored elastic energy at the beginning and the end of the event is taken as the size of the event (Fig. 23). From this energy release the model equivalent of a moment magnitude of the event (Kanamori and Anderson, 1975) can be calculated by taking the logarithm, i.e. $M_M=\log_{10}(\Delta E)$. It should be noted that this Model magnitude cannot be compared quantitatively to the magnitudes of real seismic events for two key reasons. One is that all calculations performed here are using "model units", i.e. the calculated values would need to be scaled to real world units by assigning parameters like size to the model faults, which is not done in this work. The more important reason, however, is that the models used here represent a 1D fault embedded in a 2D medium and therefore the scaling relations of real seismic events which assume a 2D fault in a 3D medium, (Kanamori and Anderson, 1975) are not applicable. However, the calculated model magnitudes can still be used to qualitatively evaluate the seismic activity of the model faults (similar to Weatherly and Abe, 2004) and in particular to compare the seismicity between different simulations.

8. Models

8.1. Simple Geometry

The aim of this part of the study was to investigate the feasibility to model the possible loading rate dependence of the dynamic behaviour of a fault containing salt using the DEM approach described above. For this purpose a parameter study

varying the loading rate and the salt rheology in a fault model using a very simple geometry was performed.

The model used for this study consists of rough planar (1D) fault embedded in a 2D elastic medium with an added block of material representing a salt lens in the centre section of the fault (Fig. 21). The length of this block is 50% of the total length of the model, its aspect ratio is 6:1. The box shape of the block was chosen to simplify the model setup. On top and bottom edges of the model a defined normal stress and shear rate are applied, both are held constant after an initial “ramp-up” phase. On the lateral sides of the model periodic boundary conditions have been applied to enable arbitrary shear displacements without a change in the large-scale geometry of the model.

A total of 8 simulations were used for the parameter study, using 4 different values for the viscosity parameter A (0.1, 0.25, 1.0 and 2.5) and a slow and a fast loading rate for each of them. The loading rates chosen were 10^{-5} model velocity units and 10^{-6} model velocity units. Given that the P-Wave velocity in the model is v_P=1.0 model unit, this would be equivalent to a few cm/s to a few mm/s depending on the rock type. This is of course a lot higher that the realistically expected long term deformation rates for natural faults, but it strikes a balance between realistic values and computational feasibility. The chosen velocities are slow enough so that the loading of the fault does not interfere with dynamic processes during slip events which happen at velocities between a few m/s (fault slip) and km/s (slip propagation). On the other hand those velocities enable the simulation of statistically valid event catalogues with several thousand slip events in a practical time on a standard multicore workstation (hours to tens of hours).

In the simulation the elastic energy stored in the material was tracked and the resulting data used to generate event size distributions for the different simulations (see section above). The results (Fig. 26-29) show that in all cases there is a clear loading rate dependence of the frequency-size distributions of the events. The simulations with the slower loading rate (10^{-6}) are producing event size distributions showing a trend towards more frequent large events. The actual size of the largest events is not increased. These observations apply independently of the salt viscosity parameter used in the models. It is important to note that the models with different loading rates were run for the same amount of total shear displacement, not the same amount of time.

This initially counterintuitive result, i.e. more large events during a given amount of fault displacement at slower loading rates, can possibly be explained by looking at the amount of elastic energy stored in the rock- and salt parts of the model during different parts of the stick-slip cycle. The data (Fig. 30, 31) shows that during inter-seismic times, i.e. the period between the events, the salt in the models stores relatively little elastic energy. The reason is that at the combination of strain rates and salt viscosity used in the models the salt has enough time between events to completely relax. Therefore the salt does not contribute to any co-seismic release of elastic energy. During and immediately after a large event, however, stress, and

therefore elastic energy, is transferred to the salt by the co-seismic movement of the adjacent "rock" (see red vs. black curves in Fig 30, 31), i.e. whenever there is a large slip event the amount of elastic energy in the salt is increased. Therefore, after a large event, slip events are suppressed, and the energy available for subsequent events is reduced. In the fast loading models (Fig. 30) the relaxation time of the salt covers a longer part of the typical inter-event time than in the slow loading runs (Fig. 31), therefore a stronger reduction in the size of the subsequent events happens in the fast runs.

This mechanism will not be applicable to models where the salt retains sufficient stored elastic energy between events to actually make a positive contribution to the energy release of the events. This would be expected in case of very high salt viscosity or high loading rates. However, this part of the parameter space has been inaccessible to the present study due to limitations of the DEM implementation used.

8.2. Complex Geometry

The aim of this part of the study was to test the feasibility of integrating more complex geometries, resembling possible realistic fault zone architectures, into the modelling approach.

For this purpose a set of models was constructed which contain a number of fault rock lenses between the two block of wall rock (Fig. 32, 33). The wall rock has the same properties as in the previous models, i.e. it consists of particles fully connected by bonded interactions. The fault rock lenses can either consist of a material identical to the wall rock or of salt (purple coloured particles in Fig 32, 33). In the models used in the present work only one of the lenses is filled with salt material, whereas the other lenses consist of rock material. On the interfaces between different fault rock lenses and between a fault rock lens and the wall rock the particles interact by breakable bonded interactions similar to those within the rock material, but with a much lower breaking strength. In the models used in the present work the cohesion of the inter-lens bonds was set to 0.0003 model stress units which, assuming elastic properties of typical crustal rocks as scaling parameters, would be equivalent to cohesion of ~10MPa, therefore representing a plausible strength level for a partially healed fault surface.

In contrast to the previous set of models (section 2.1) the simulations are only run to smaller amount of shear displacement. This is due to the fact that in contrast to the previous simulations which sought to explore the statistics of the “steady state” behaviour of a pre-existing fault the simulations in this section are targeting the transient behaviour of a partially healed fault during fault reactivation, i.e. while the weakly bonded connections between the individual lenses of fault rock are breaking.

A total of 8 simulations has been run for this section, using two different model setups an three different values for the salt viscosity (a=0.25, a=1.0 and a=2.5) each. In addition, the models with a viscosity parameter a=1.0 where run using two different shear loading rates, $v=10^{-5}$ and $v=10^{-6}$. The two model setups differ only in the choice which of the fault lenses was set up to contain salt instead of fault rock. In the first

model (Fig. 32) a lens spanning about half the width of the model was chosen whereas in the second model (Fig. 33).
The results show that the mode of deformation in the complex fault models strongly depends on the distribution of the salt within the fault. In the fault model where the salt lens covers only about half of the total length of the fault zone (Fig. 32) the deformation is localized at a number of the weak interfaces between different fault rock lenses (Fig. 34, strong colour contrasts show localized deformation). In contrast, if the salt forms a layer spanning the whole length of the fault zone (i.e. Fig. 33) the deformation is almost entirely contained within the salt layer and the interface between the salt layer and the fault rock (Fig. 35). As a consequence of the different deformation distribution the dynamic behaviour of the two models differs strongly. The model with a continuous salt layer exhibits low strength and a nearly aseismic creep (Fig. 36, blue and magenta curve, Fig. 38) whereas the model with a salt lens covering only part of the length of the fault zone shows much higher strength and a pronounced stick-slip behaviour (Fig. 36, red and black curve, Fig. 37). Plots of the variation in the shear force needed to maintain a constant shear rate of the fault (Figs. 36-38) show that the dynamic behaviour of the fault models depends on the loading rate and the viscosity of the salt in these simulations too. In the model with a continuous salt layer the differences are restricted to a small variation in the overall strength of the fault (Fig. 36, blue and magenta curve, Fig. 38). In the other models a change in timing, size and number of the stick-slip events can be observed (Fig. 36, red and black curve, Fig. 37).

9. Conclusions / Outlook

The results of the present study have shown that the DEM approach is in principle suitable for the modelling of the seismicity of faults containing salt or other ductile materials. Initial tests have shown that the presence of salt in a fault zone has the potential to make the dynamic behaviour of the fault dependent on shear loading rate, including the modification of the frequency magnitude distribution of the generated seismic events. While some trends have become visible, large parts of the parameter space of fault geometry, salt rheology and loading rate remain unexplored and the complex interplay between stick-slip dynamics of a fault and the visco-elastic behaviour of the salt contained in it is not really understood so far.
In order to enable a more quantitative investigation of the influence of salt on the dynamic behaviour, in particular with regard to the details of the rheology of the salt, an extension of the method used would be needed. Possible avenues in that direction would be the implementation of a Maxwell material instead of a Voigt-Kelvin material at the particle scale into the DEM formalism or a coupling between the DEM approach and a Smooth Particle Hydrodynamic (SPH) model. The latter approach has been shown the be feasible (Komoróczi et al., 2013, Robinson et al., 2014) and to be applicable to the modelling of coupled brittle-ductile problems ((Komoróczi et al., 2013)

10. References

Abe, S., Place, D., and Mora, P., 2003. A parallel implementation of the lattice solid model for the simulation of rock mechanics and earthquake dynamics. Pure Appl. Geophys., 161. 2265–2277

Abe, S., Latham, S. and Mora, P., 2006, Dynamic Rupture in a 3-D Particle-based Simulation of a Rough Planar, Fault, Pure Appl. Geophys., 163, 1881-1892

Abe, S. and Urai, J.L., 2012, Discrete element modeling of boudinage: Insights on rock rheology, matrix flow, and evolution of geometry, J. Geophys. Res., 117, B01407

Cundall, P.A., and Strack, O., 1979. A discrete numerical model for granular assemblies. Geotechnique, 29, 47–65.

Fournier, T., and Morgan, J., 2012, Insights to slip behavior on rough faults using discrete element modelling, Geophys. Res. Lett., 39, L12394

Kanamori, H. and Anderson, D.L., 1975, Theoretical basis of some empirical relations in seismology, Bull. Seis. Soc. Am., 65(5), 1073-1095

Komoróczi, A., Abe, S., and Urai, J.L., 2013, Meshless numerical modeling of brittle–viscous deformation: first results on boudinage and hydrofracturing using a coupling of discrete element method (DEM) and smoothed particle hydrodynamics (SPH), Comp. Geosci., 17, 373–390

Mora, P. and Place, D., 1994. Simulation of the frictional stick–slip instability. Pure Appl. Geophys. 143, 61–87.

Place, D., Mora, P., 1999. The lattice solid model: incorporation of intrinsic friction. J. Comp. Phys. 150, 332–372.

Potyondy, D., Cundall, P., 2004. A bonded-particle model for rock. Int. J. Rock Mech. Min. Sci., 41 (8), 1329–1364

Robinson, M., Ramaioli, M. and Luding, S., 2014, Fluid–particle flow simulations using two-way-coupled mesoscale SPH–DEM and validation, Int. J. Multiph. Flow, 59, 121-134

Wang, Y., Abe, S., Latham, S., Mora, P., 2006. Implementation of particle-scale rotation in the 3-d lattice solid model. Pure Appl. Geophys., 163, 1769–1785.

Aspects of fault zones around the Rotliegend reservoirs and the possible effects of salt in the fault zones on rates of seismicity in these zones

Figure slides accompanying the written report

Janos L. Urai (1), Michael Kettermann (1), Streffen Abe (2), Simon Virgo (1)

(1)
Structural Geology, Tectonics and Geomechanics
RWTH Aachen University,
Lochnerstrasse 4-20
D-52056 Aachen, Germany
www.ged.rwth-aachen.de

(2)
Institut für geothermisches Ressourcenmanagement
Berlinstr. 107a
D-55411 Bingen
www.igem-energie.de

Supervision:
ir J.P.A.Roest, State Supervision of Mines, Ministerie van Economische Zaken,
Henri Faasdreef 312 | 2492 JP | Den Haag

Analogue modeling of salt intrusion into dilatant faults

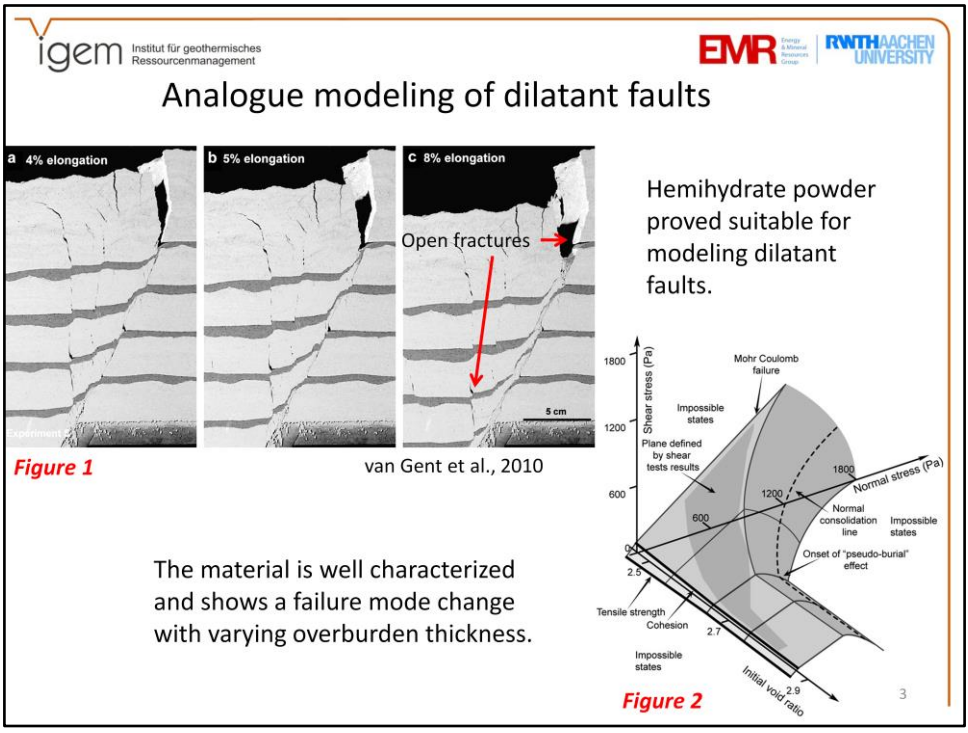

Figure 1: Example of an experiment showing that hemihydrate powder (white layers) is suitable to model dilatant faults (van Gent et al, 2010). Darker layers have lower cohesion. Notice the open fractures throughout the fault zone.

Figure 2: Material characterization of hemihydrate powder (van Gent et al, 2010).

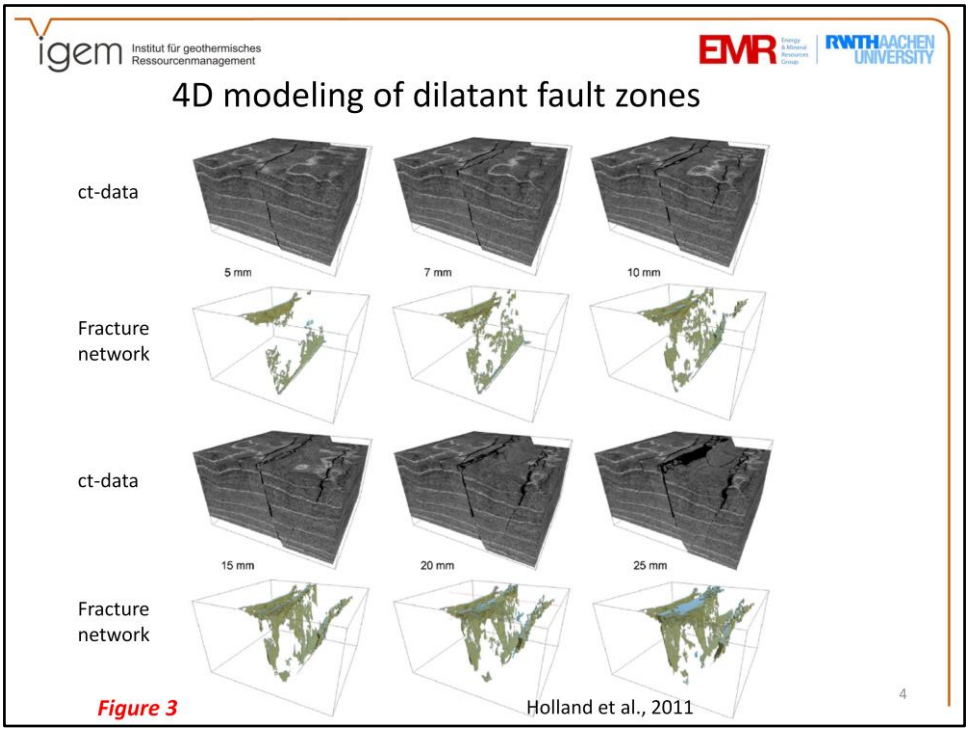

Figure 3: Subsequent ct-scans of experiments of normal faulting in hemihydrate powder show a complex network of open fractures (Holland et al., 2011)

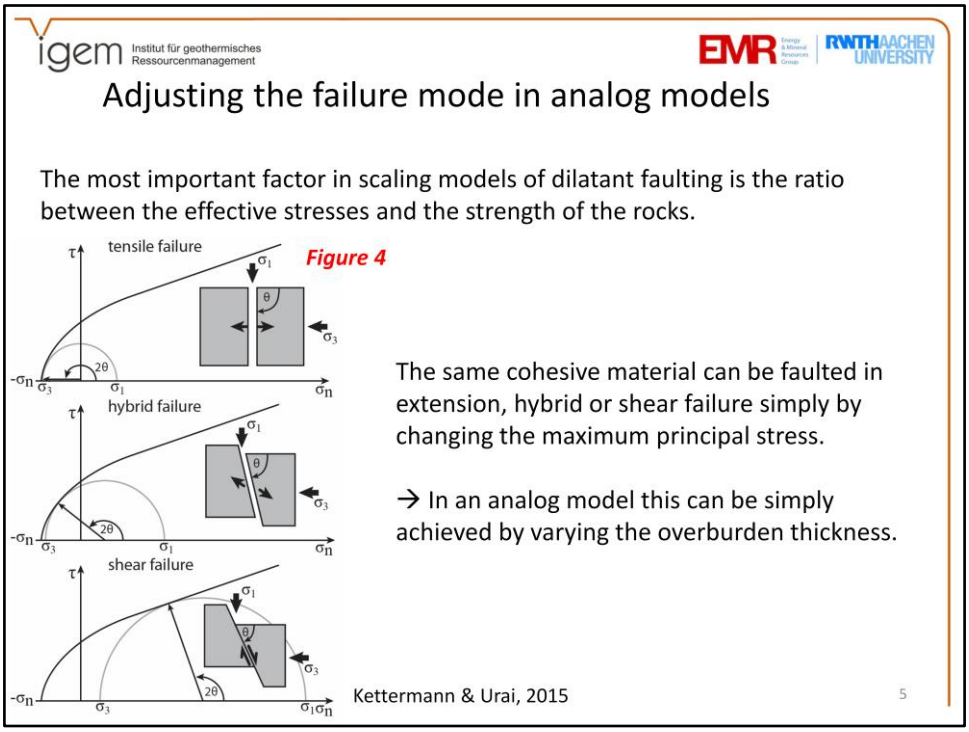

Figure 4: Mohr-Coulomb failure criteria for tensile, hybrid and shear failure. Tensile and hybrid failure require small maximum principal stresses (σ1).

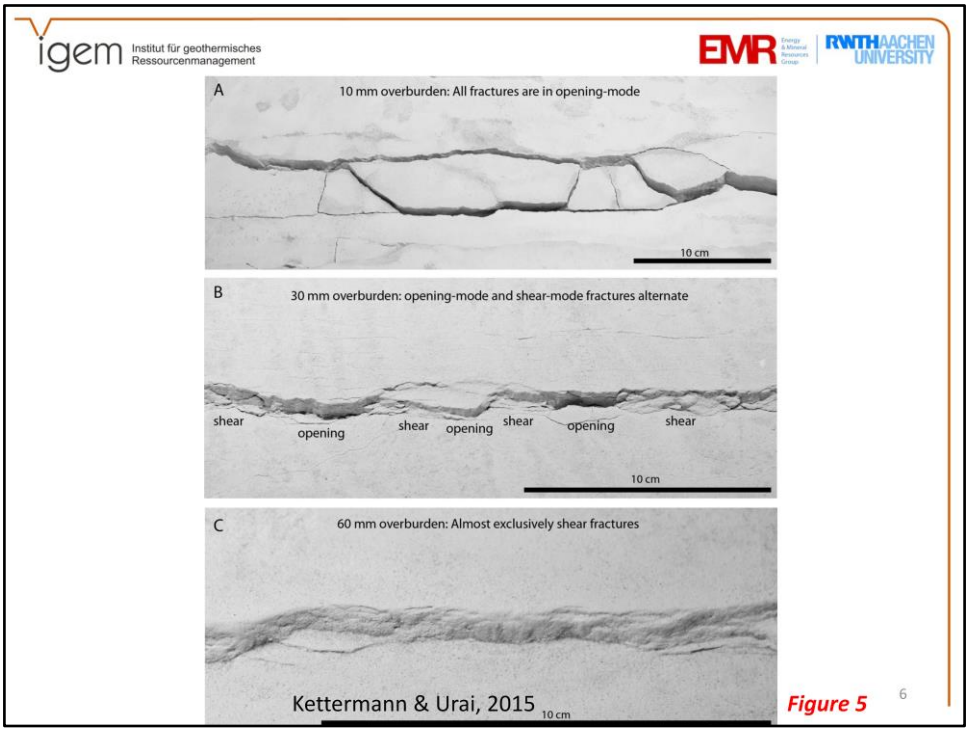

Figure 5: Characteristic geometries of normal faults in tensile (A), hybrid (B) and shear failure (C) as shown by Kettermann and Urai (2015). Note the massively dilatant fractures in (A) and still pronounced open fractures in the hybrid failure case (B).

Experiment idea

We combine cohesive powders as analog for brittle rocks and ductile material as salt analog in dynamic models.

To maximize the outcome of this project we use two approaches:

(1) Using a hardening resin as salt analog allows post mortem investigation of the 3D structure of salt that has entered open fractures.

(2) A transparent salt analog allows 3D observations of fault formation. Hardening the powder post mortem allows detailed investigation of the fault zone itself.

We vary the basement fault angle (63° and 70°) to cover a range of possible fault zone geometries.

Assumptions

1. The salt is viscous
2. The salt has enough time to flow into the faults
3. Rocks beneath the salt are faulted in extensional or hybrid failure

Dimensions and scaling

- The basic idea of these models derive from the Groningen area. The models stratigraphy is therefore chosen to roughly represent the natural stratigraphy in a length-scale of 1:10000. The width of the deformation box is 30 cm.

- As faults in the Permian anhydrites and carbonates beneath Z3 andZ4 salts are expected to have formed during and after the deposition of the Zechstein salts, we expect hybrid or extensional faulting.

  → We adjust the overburden pressure in the models so that the used powder fails accordingly, by using only thin layers of overlying salt analog

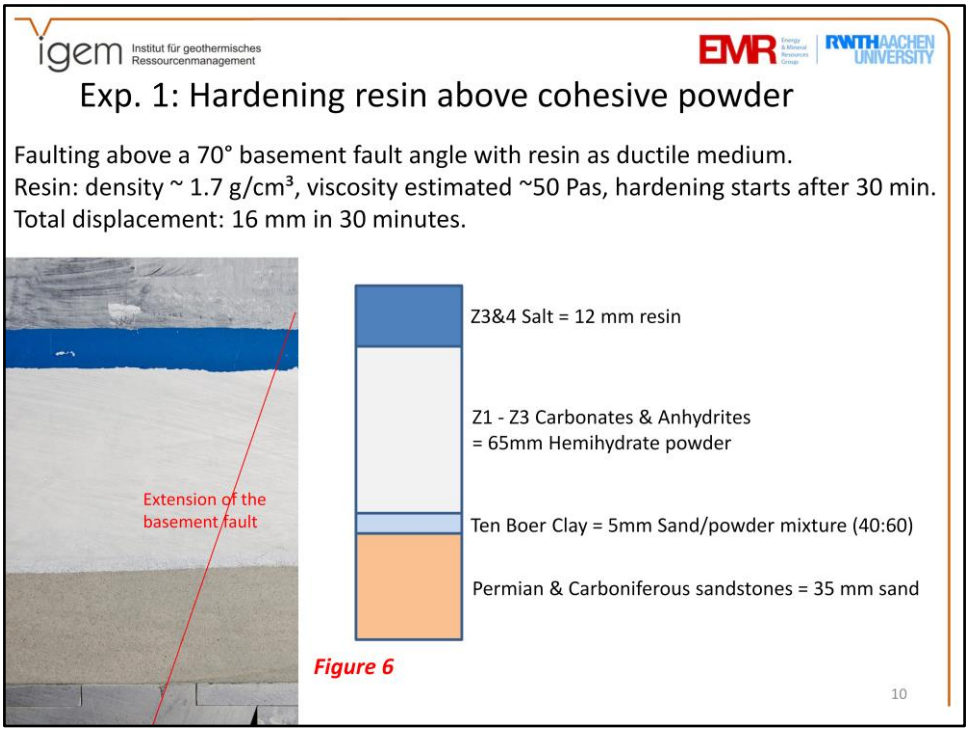

Figure 6: Initial setup of experiment 1: 35 mm of sand represent Permian and Carboniferous sandstones (sand), covered by 5 mm of a sand-powder mixture (light blue) representing the Ten Boer Clay. The Z1 - Z3 carbonates and anhydrites are represented by 65 mm hemihydrate powder (white) and finally covered by 12 mm resin (blue) as analog for the Z3 and Z4 salt. A red line shows the elongation of the 70° basement fault.

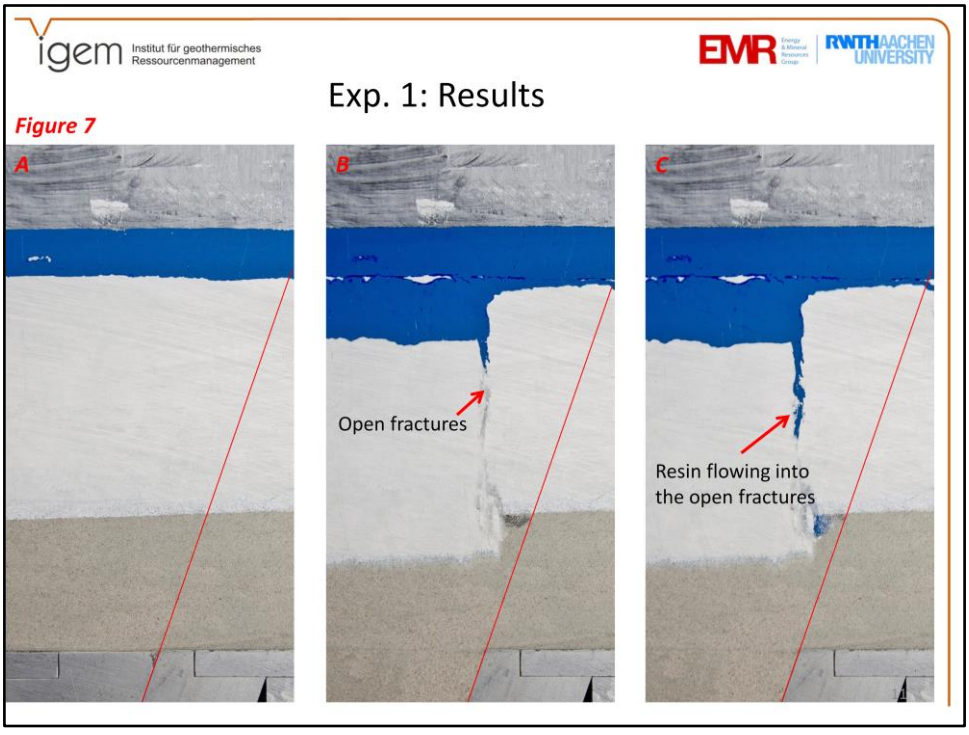

Figure 7: Three images at different stages of the deformation. Open fractures formed between (a) and (B) are subsequently filled with the blue resin. The resin continues flowing downwards into the fault even after the faulting stopped (compare B and C). A red line shows the elongation of the 70° basement fault.

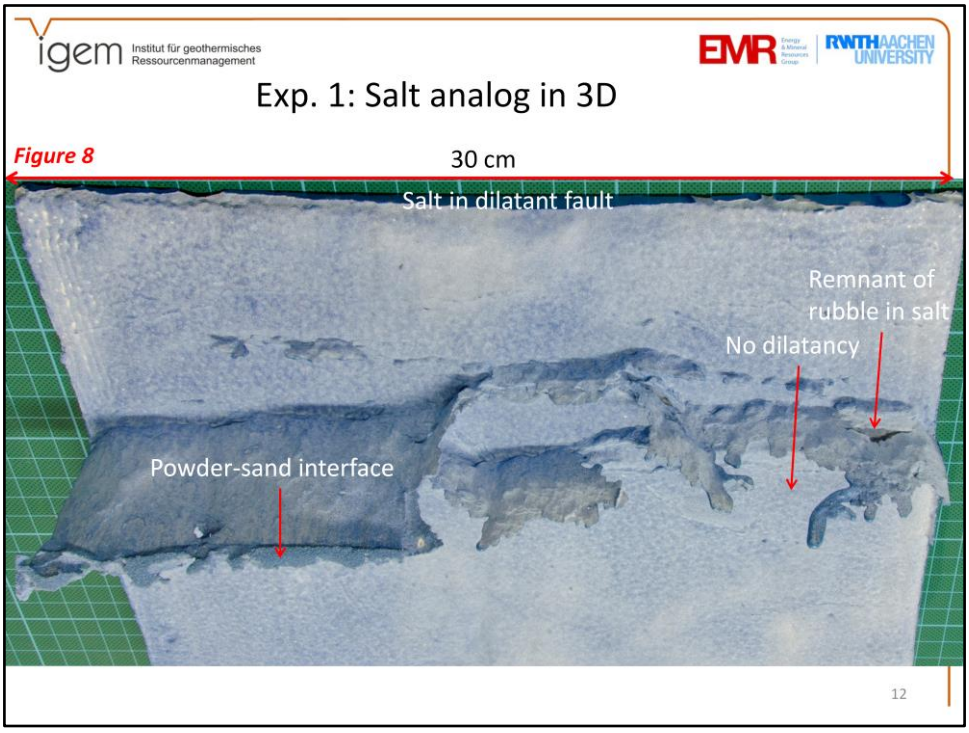

Figure 8: The excavated hardened resin show the distribution of ‘salt in the fault’. On the left side the resin reached the salt powder interface and accumulated there. On the right side the resin has not flown down so far. Larger parts of the fault were not dilatant and hence there was no space for the resin to flow into. Fragments of the powder that fell into the resin left open cavities.

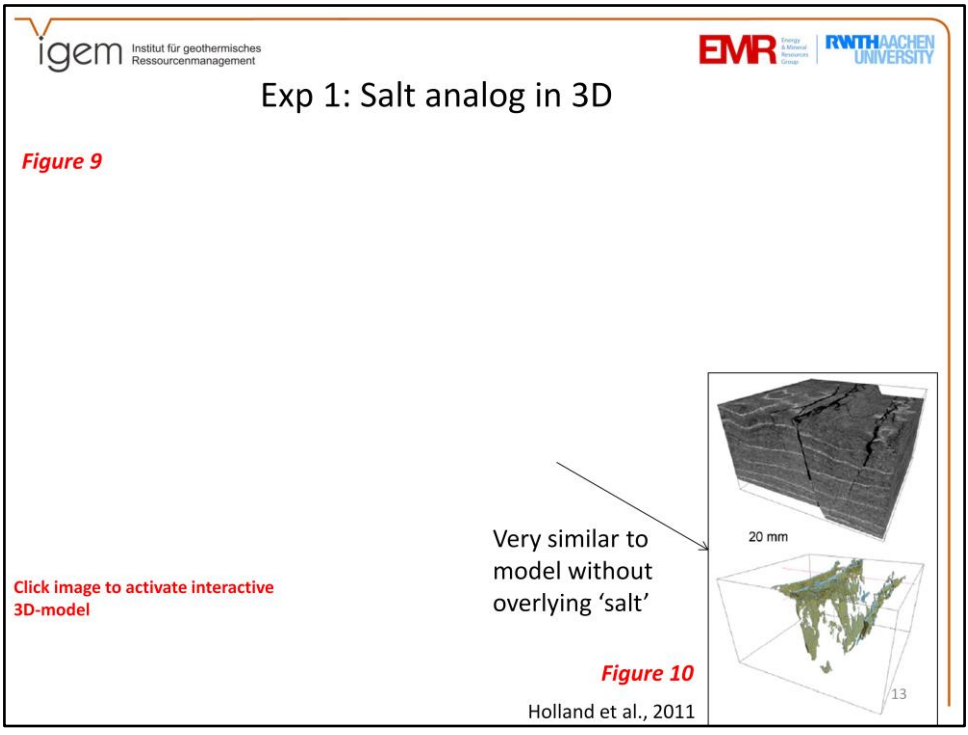

Figure 9: The 3D model of the hardened resin shows remarkable similarity with the experiments of Holland et al. (2011) that were performed without a ductile overburden (Fig. 10). Click on the image (Fig. 9) to activate the interactive 3D model. Pivot with the left mouse button and zoom with the scroll wheel.

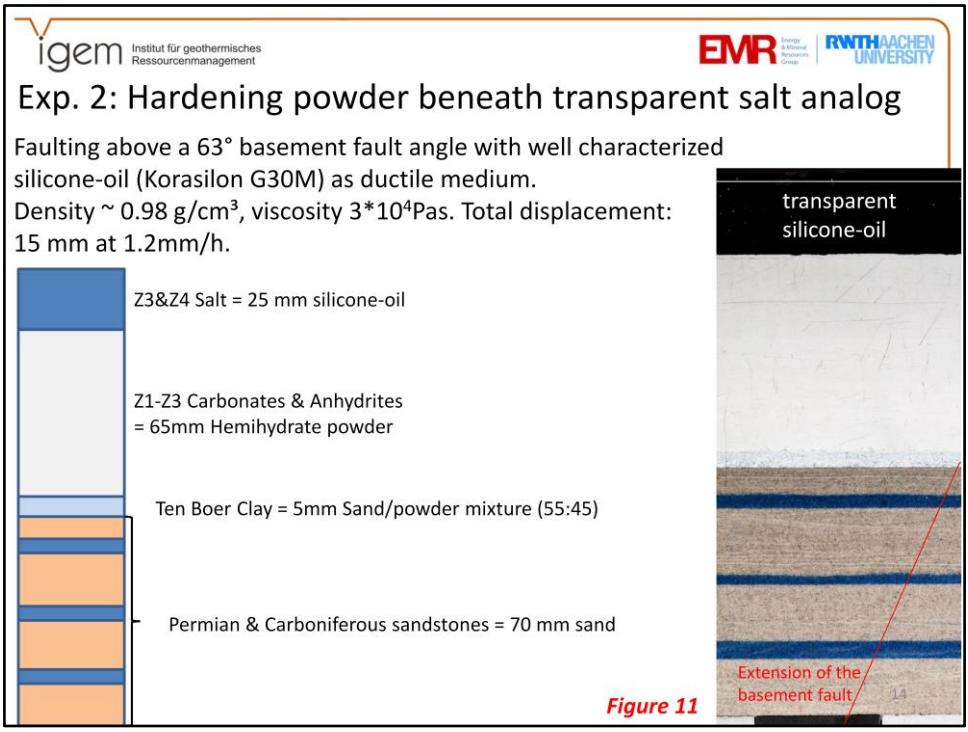

Figure 11: Initial setup of experiment 2: : 70 mm of sand represent Permian and Carboniferous sandstones (alternating gray and blue sand), covered by 5 mm of a sand-powder mixture (light blue) representing the Ten Boer Clay. The Z1 - Z3 carbonates and anhydrites are represented by 65 mm hemihydrate powder (white) and finally covered by 25 mm transparent silicone-oil as analog for the Z3 and Z4 salt. A red line shows the elongation of the 63° basement fault.

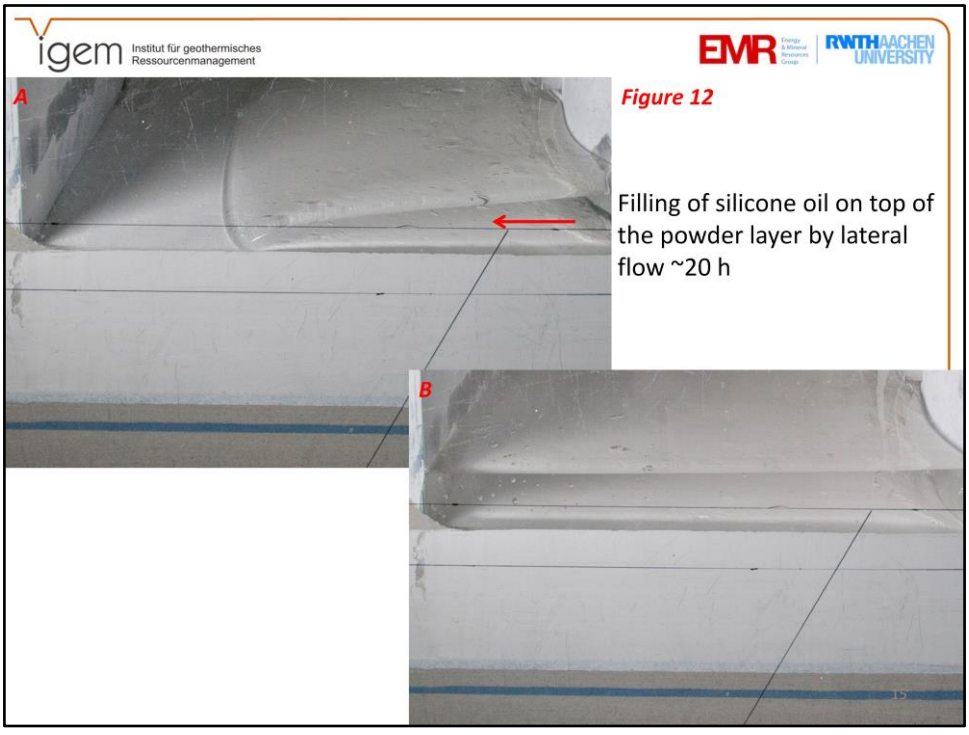

Figure 12: Photos show the process of filling the silicone oil on top of the highly sensitive powder layer. Over the course of 20 h the silicone-oil was allowed to flow over the surface from one side and equilibrate. Black lines on the glass helped to set up the experiment and were removed before the deformation was started.

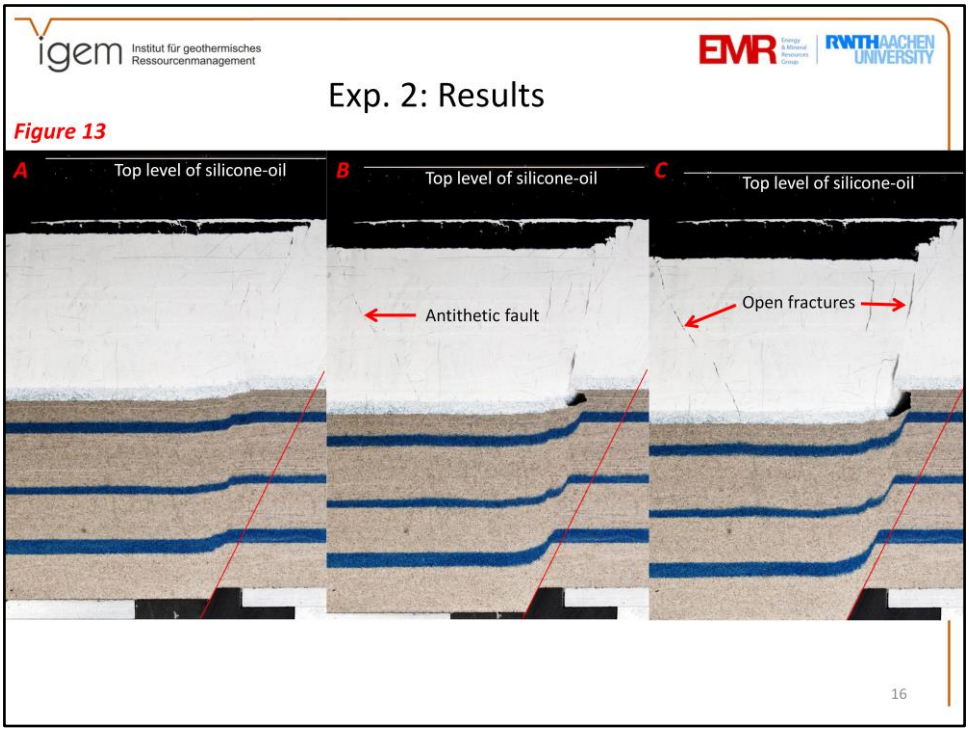

Figure 13: Three stages of faulting of experiment 2. The transparent silicone-oil is almost invisible in side-view and therefore the top-level is marked by white lines. Red lines shows the elongation of the 63° basement fault.
Compared to the first experiment with 70° basement fault angle, faults are now shallower and an antithetic fault formed (see B and C).

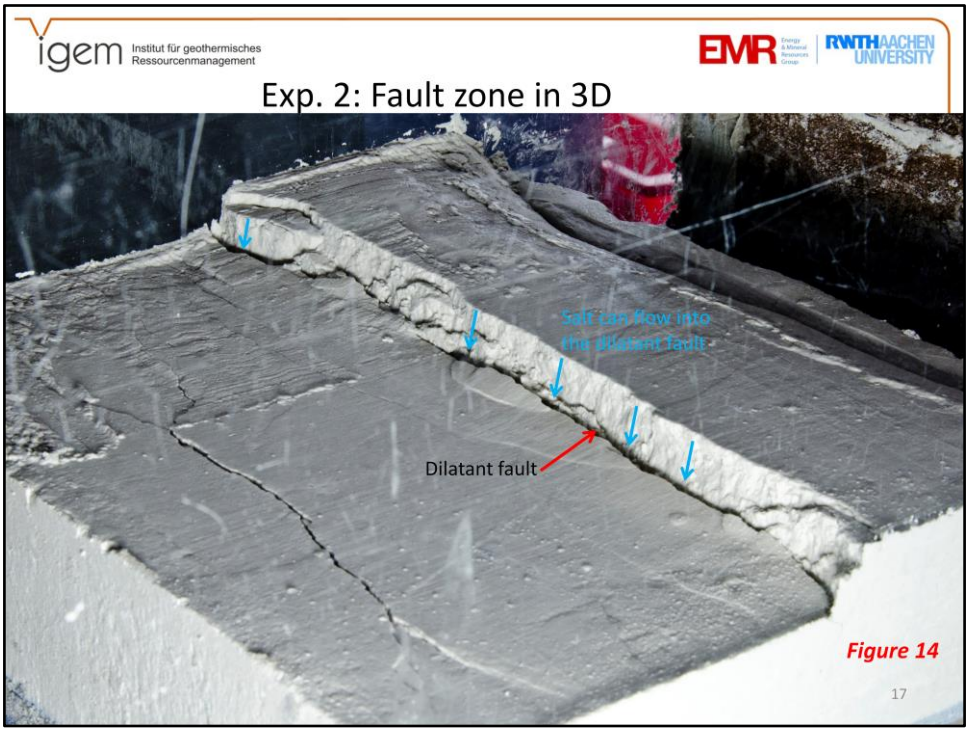

Figure 14: This photo was taken after the silicone-oil layer was removed and shows the now hardened powder layer. One could imagine this to be the top Z3 Anhydrite. Shadows show the dilatancy at the fault, were salt-analog flowed into the fault.

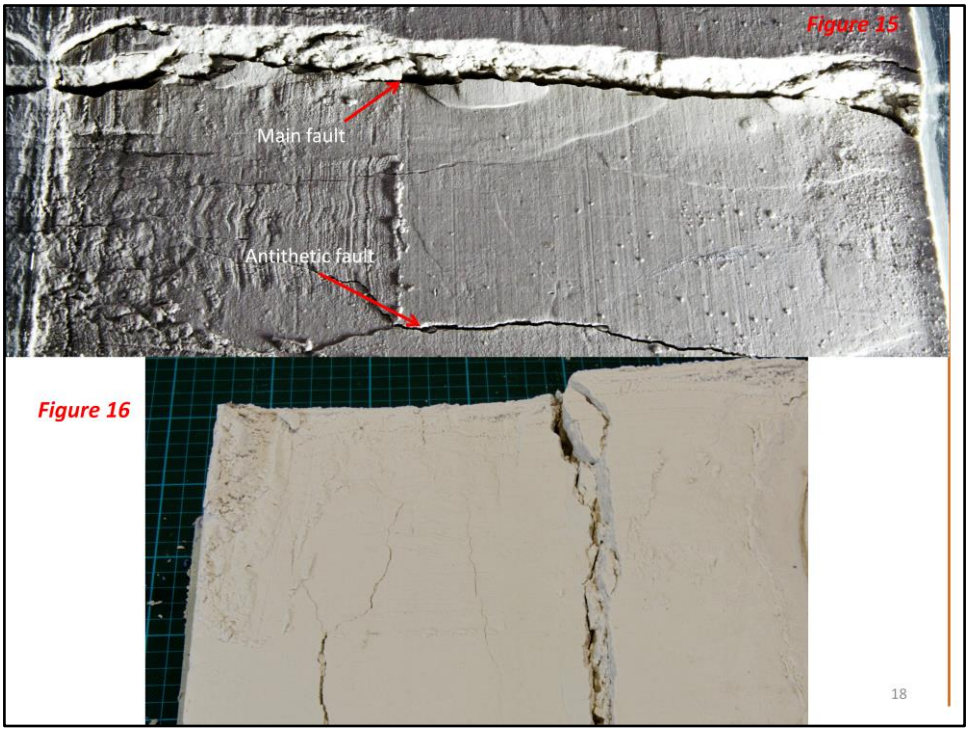

Figure 15: The top-view photo shows the open fractures at the main fault and the antithetic fault. Both were filled with silicone-oil.

Figure 16: View directly into the open fractures that reach deep down along the fault and were filled with silicone-oil.

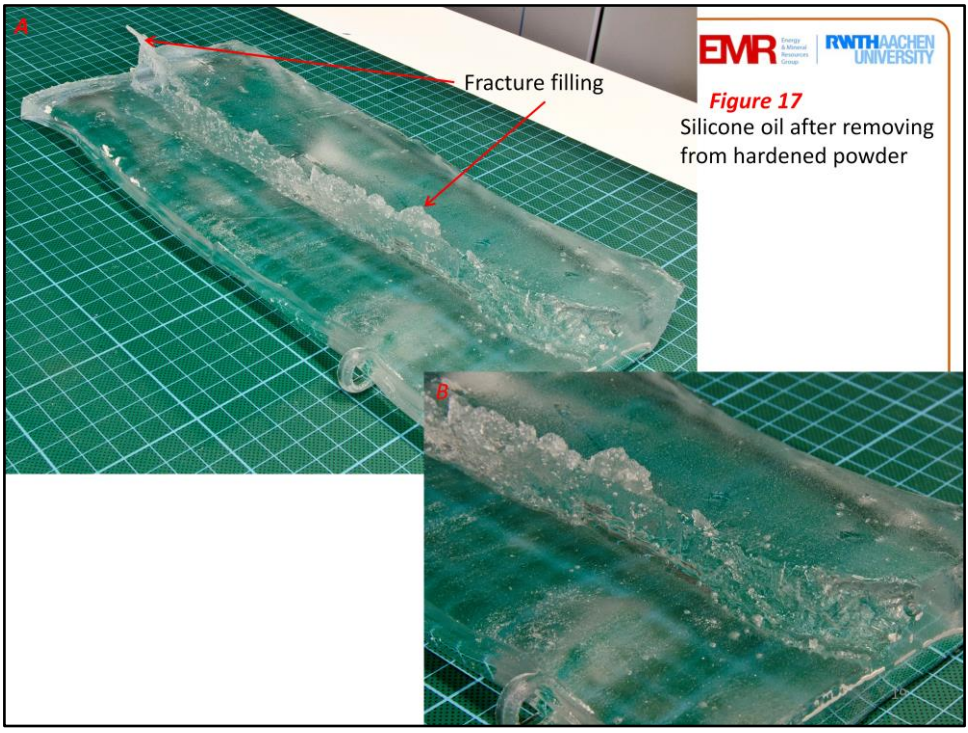

Figure 17: The silicone-oil immediately after removing it. It shows a negative of the fracture system, silicone-oil that was inside open fractures now stands out. However, a distinct portion of the silicone-oil teared off during removal as it interlocked with the complex fracture surface.

DEM Modelling of the stick-slip dynamics of Faults containing Salt

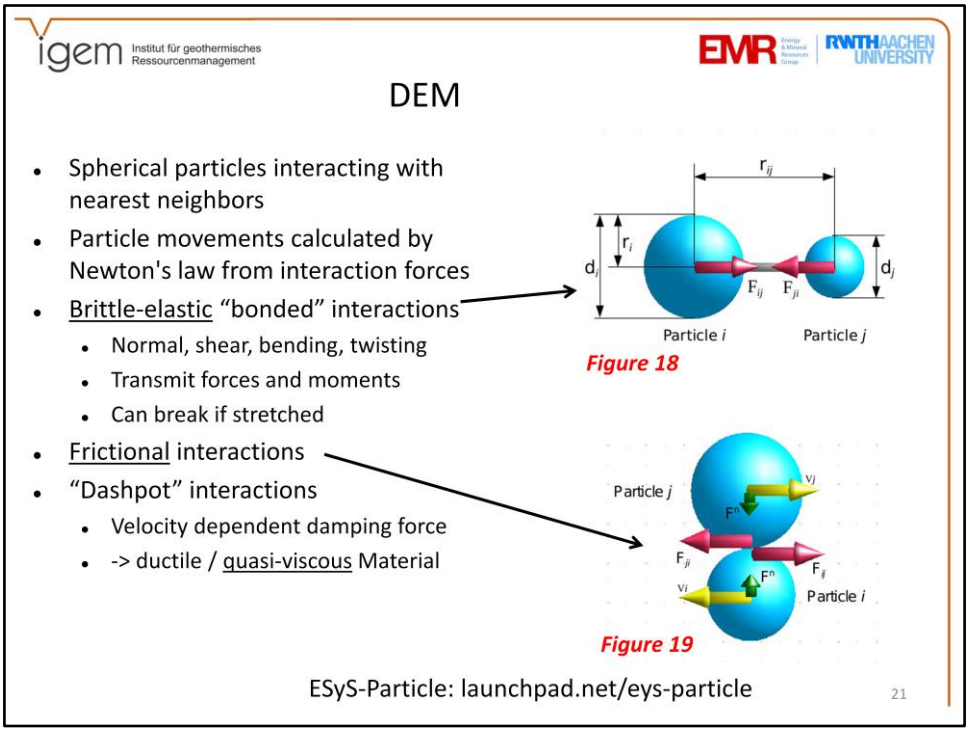

Figure 18: Schematic drawing of two particles interacting by a brittle-elastic "bonded" interaction. r_i is the radius of particle i, r_{ij} is the current distance between the particles and F_{ij} is the force applied to particle i by the interaction with particle j

Figure 19: Schematic drawing of two particles interacting by a frictional interaction. Here F_{ij} is the tangential force applied to particle i by the frictional interaction with particle j, whereas F^n is the normal force between the particles which is due to an elastic interaction acting in parallel with the frictional interaction.

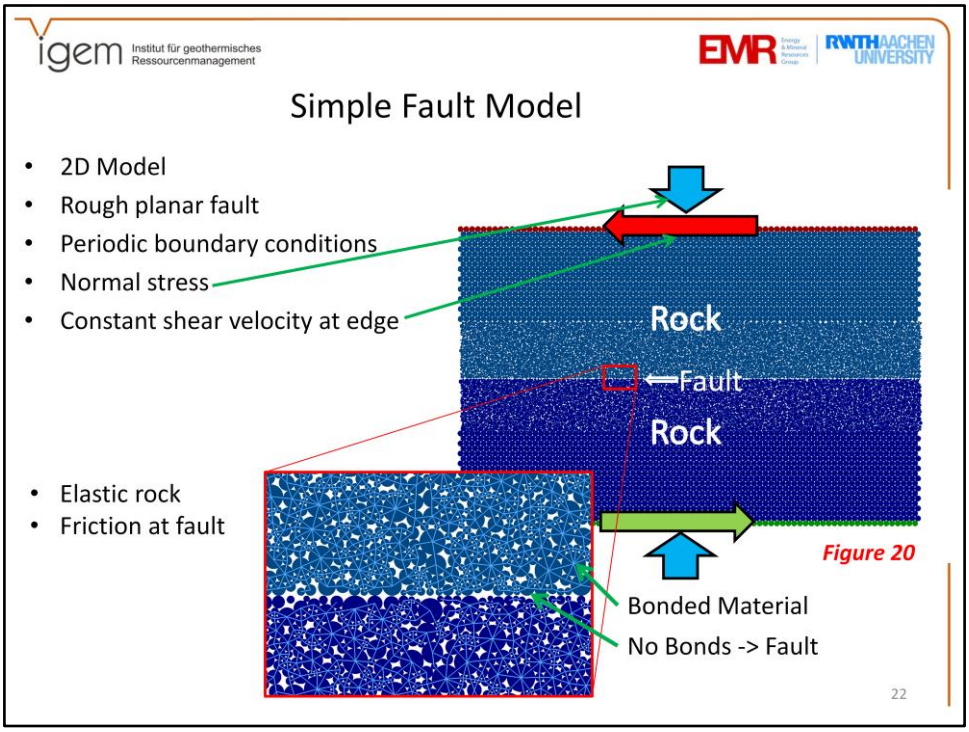

Figure 20: Simple DEM fault model without salt. The blue colored particles form two blocks in which the particles are bonded together, but there are no bonds between the two blocks, i.e. between the light blue and the dark blue particles. The interface between the two blocks therefore forms a rough fault where the particles interact by frictional interactions. The red / green rows of particles at the outer edges are connected to the respective driving plates used to impose a shear displacement and a normal stress to the model.

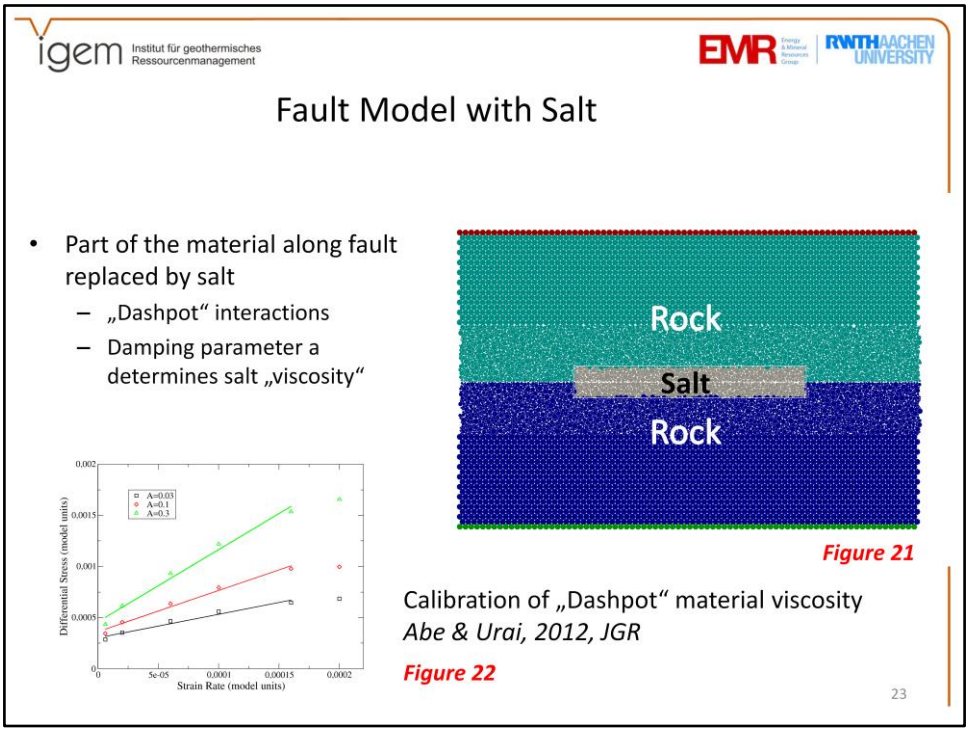

Figure 21: DEM fault model with salt. As in Figure 3, the blue / turqouise colored particles form two blocks in which the particles are bonded together, but there are no bonds between the two blocks. The gray particles represent the salt, i.e. the interactions between the gray particles and between a gray particles and another particle are implemented as a combination of elastic repulsion and velocity-dependent damping.

Figure 22: Calibration of the rheology of the “dashpot” material (adapted from Abe & Urai 2012). Open symbols show the differential stress observed in simulations of a pure shear experiment depending on the strain rate imposed on the material. The different colors show the data for materials using different values of the damping coefficient A (black A=0.03, red A=0.1, green A=0.3). The solid lines show linear fits to the data for a strain rate below 0.00016 model units.

Seismic Events

- Direct moment calculation from energy release
  - In Model units
- „Model magnitude“ $M=\log_{10}(\Delta E)$
- Automatic event detection
  - “leaky integrator” algorithm
  - *Weatherley & Abe, 2006 Nonlin. Proc. Geoph*

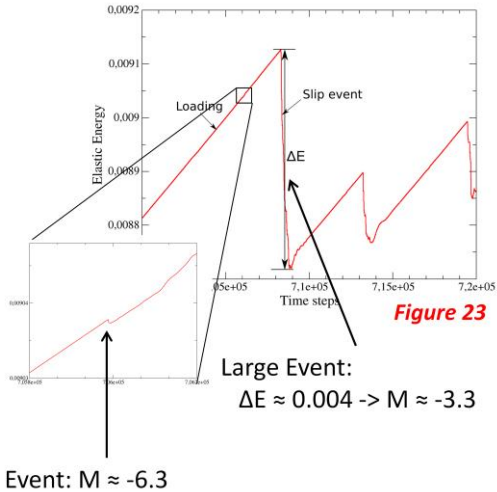

Figure 23

Large Event:
ΔE ≈ 0.004 -> M ≈ -6.3

Small Event: M ≈ -6.3

Figure 23: Elastic energy stored in the model during several stick-slip cycles. While the fault is locked the shear loading of the model leads to a steady increase of the elastic energy stored in the model which is released during slip events. The “drop” in elastic energy characterizes the size of the event. A “Model magnitude” for the events is calculated as the logarithm of the released elastic energy.

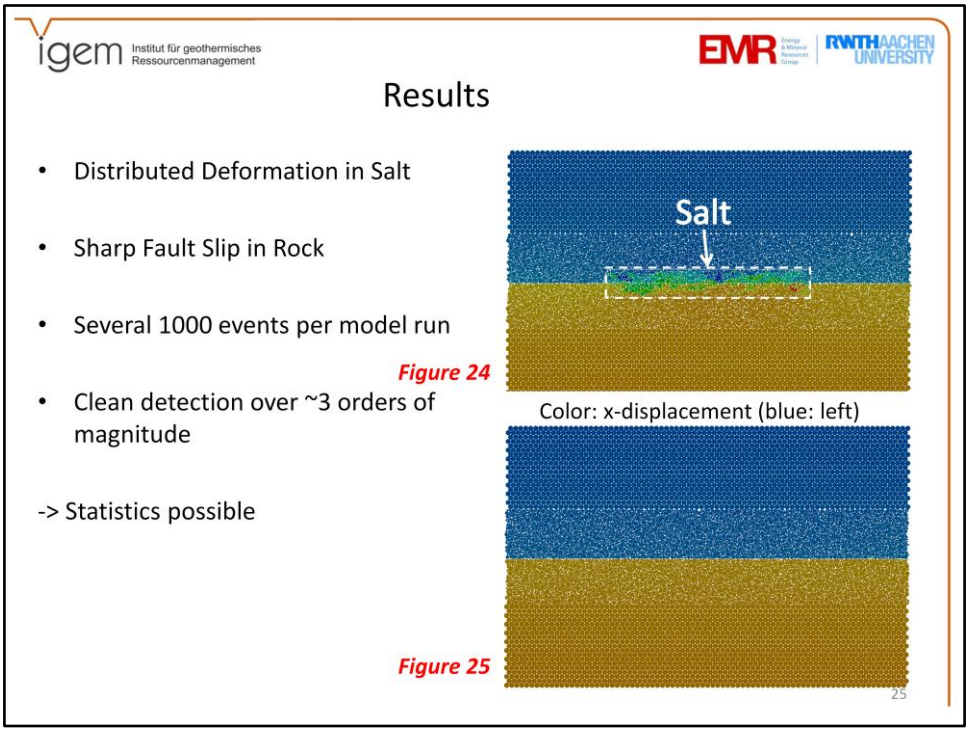

Figure 24: Deformation pattern of the fault model with a salt block included. It can be seen that the upper block is moved to the left (blue color) whereas the lower block is moved to the right (orange color). Along the sections of the fault which juxtapose rock against rock there is a sharp transition between left (-x) and right (+x) displacement, i.e . localized deformation along the fault line. In the central section of the fault which is covered by the salt block (outlined by the dashed white line) there is a smooth, irregular transition between +x and –x displacement, showing distributed deformation in the salt block.

Figure 25: Deformation pattern of the fault model without salt. A sharp transition between left (-x) and right (+x) displacement is visible along the whole length of the fault.

Simulations

Set 1:

- 50% Salt
- 2 velocities each
- 3 values for salt viscosity

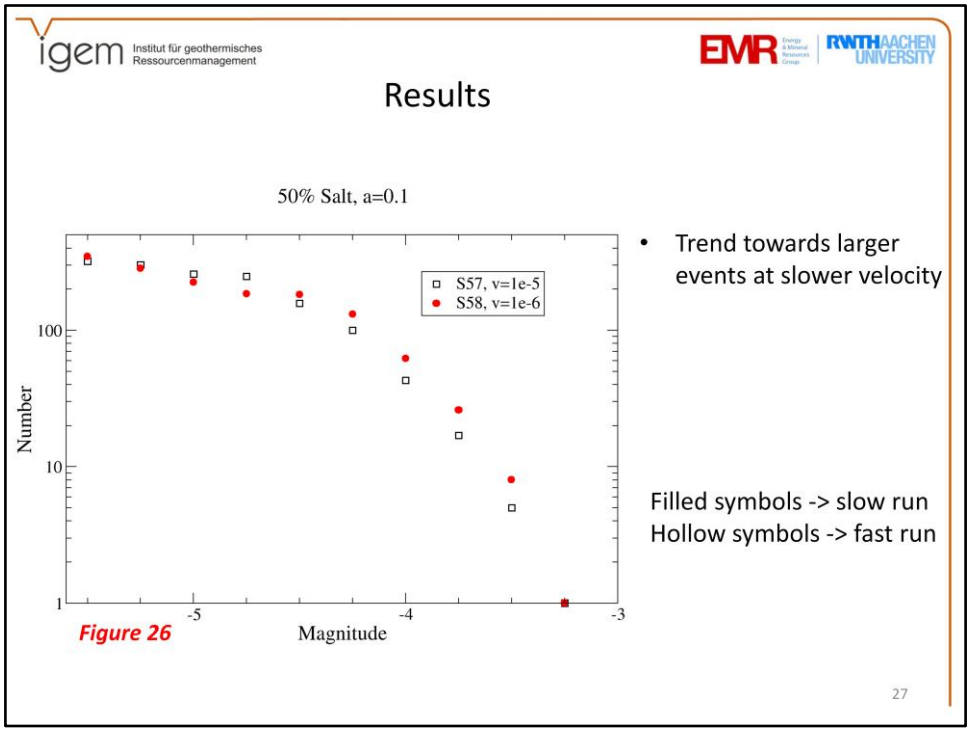

Figure 26: Frequency-magnitude distribution of the seismic events detected during a simulation using a fault with a salt block (Fig. 4) for a viscosity parameter a=0.1 for two different velocities. Symbols show the number of events within a given magnitude bin. Filled symbols show the slower of the two runs ($v_{load}=10^{-6}$) whereas the hollow symbols show the faster run ($v_{load}=10^{-5}$) .

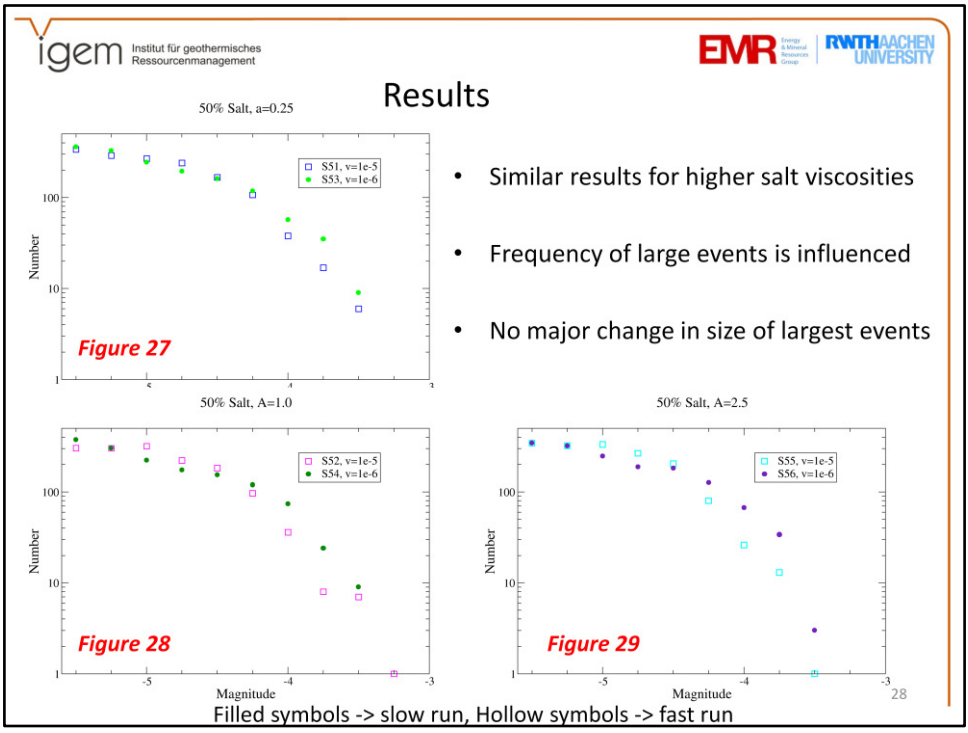

Figure 27: Frequency-magnitude distribution of the seismic events detected during a simulation using a fault with a salt block (Fig. 4) for a viscosity parameter a=0.25. Filled symbols show the slower of the two runs ($v_{load}=10^{-6}$) whereas the hollow symbols show the faster run ($v_{load}=10^{-5}$) .

Figure 28: Frequency-magnitude distribution of the seismic events detected during a simulation using a fault with a salt block (Fig. 4) for a viscosity parameter a=1.0. Filled symbols show the slower of the two runs ($v_{load}=10^{-6}$) whereas the hollow symbols show the faster run ($v_{load}=10^{-5}$) .

Figure 29: Frequency-magnitude distribution of the seismic events detected during a simulation using a fault with a salt block (Fig. 4) for a viscosity parameter a=2.5. Filled symbols show the slower of the two runs ($v_{load}=10^{-6}$) whereas the hollow symbols show the faster run ($v_{load}=10^{-5}$) .

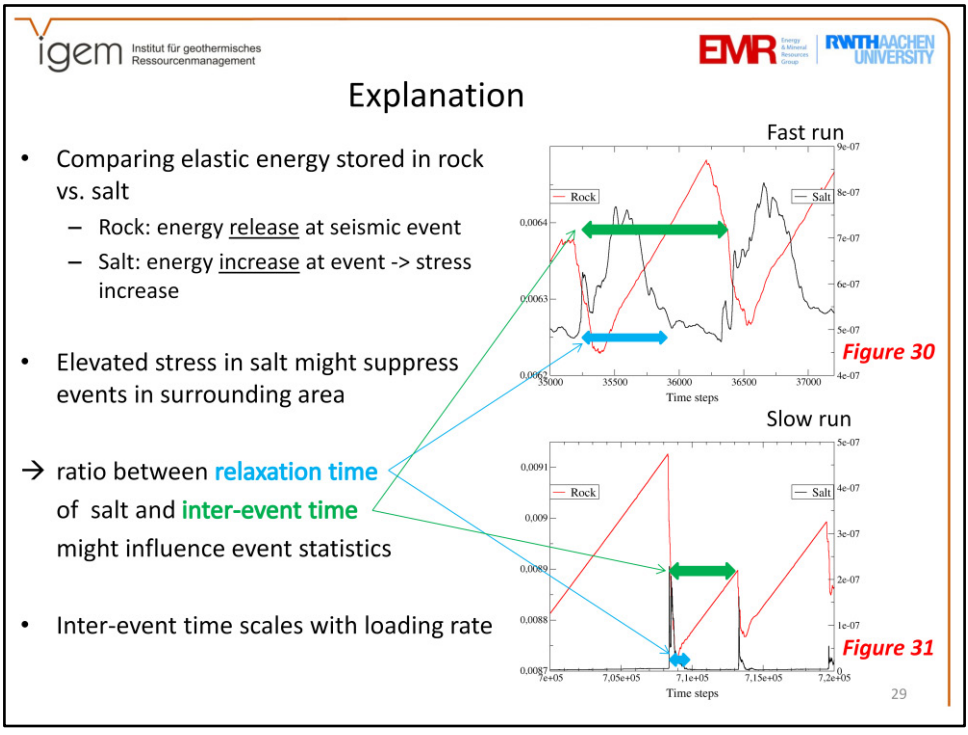

Figure 30: Evolution of stored elastic energy in the rock part of the model (red curve) and the salt part of the model (black curve) over 2 large slip events. N.B. the curves are plotted against different y-axes, i.e. the scale at the left y-axis apply to the rock (red) data, the scale at the right y-axis to the salt (black) data. Data show that for the given parameters (a=0.25, $v_{load}=10^{-5}$) the time needed to relax the salt back to its equilibrium state (blue arrow) is roughly comparable to the time between major seismic events (green arrow).

Figure 31: : Evolution of stored elastic energy in the rock and salt part of the model for a model with slower loading rate than in Fig. 14 (a=0.25, $v_{load}=10^{-6}$). In this case the relaxation time of the salt is much shorter than the inter-event time.

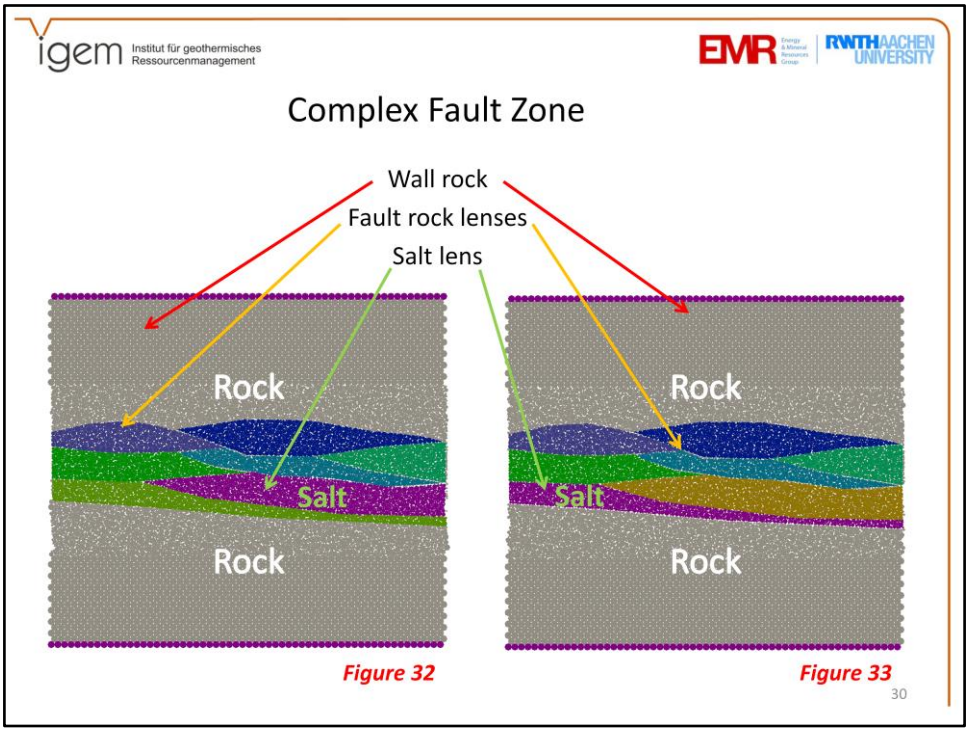

Figure 32: 2D DEM model of a more complex fault zone containing a salt lens. Gray colored particles form two blocks in which the particles are bonded together, representing the wall rocks. Colored particles in the center of the model, except purple, represent lenses of fault rock. The purple particles represent the salt lens. The bonds between the the different lenses and between the lenses and the wall rock are weaker than the bonds with in the lenses or the wall rock.

Figure 33: 2D DEM model of a more complex fault zone containing a salt lens / layer spanning the whole width of the model. The color scheme for the particles is the same as in Fig. 15, i.e. the purple colored particles represent the salt.

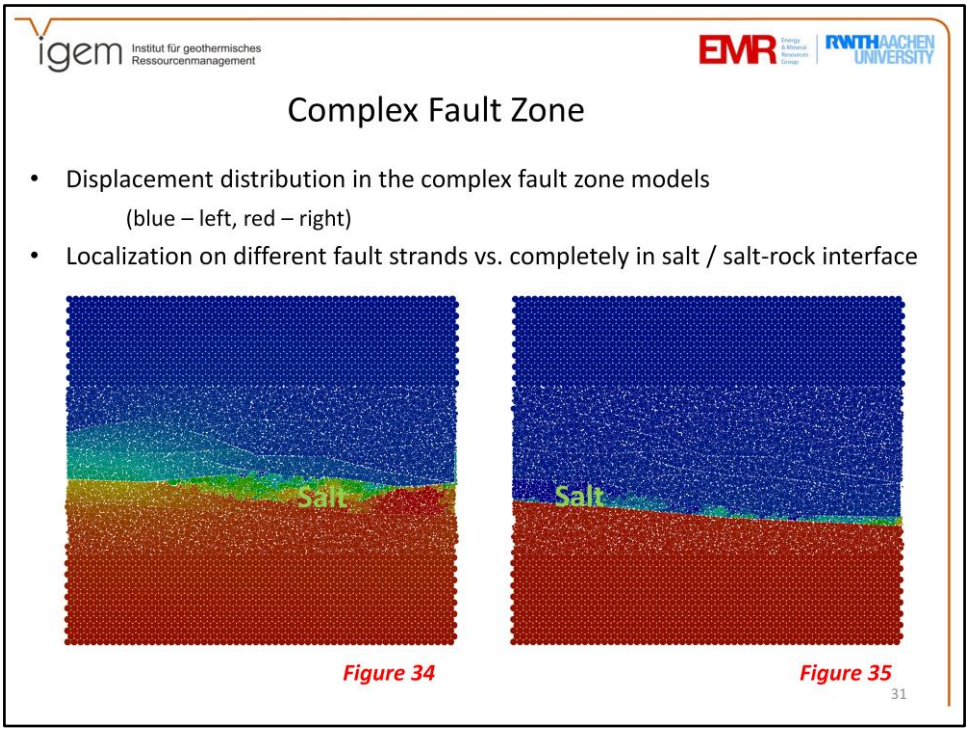

Figure 34: Distribution of x- (horizontal) displacement in a model of a more complex fault zone containing a salt lens (Fig. 15) . Colors show the displacement of the particles, red shows displacement to the right, blue to the left. Color contrasts show that the deformation is localized along multiple interfaces between fault rock lenses whereas inside the salt lens distributed deformation can be seen.

Figure 35: Distribution of x- (horizontal) displacement in a model of a more complex fault zone containing a salt lens / layer spanning the whole width of the model (Fig. 16). The color scheme for the particles is the same as in Fig. 17. In this case the color contrasts show that almost all deformation occurs distributed inside the salt (right hand side of the model) or along the salt-rock interface (left hand side).

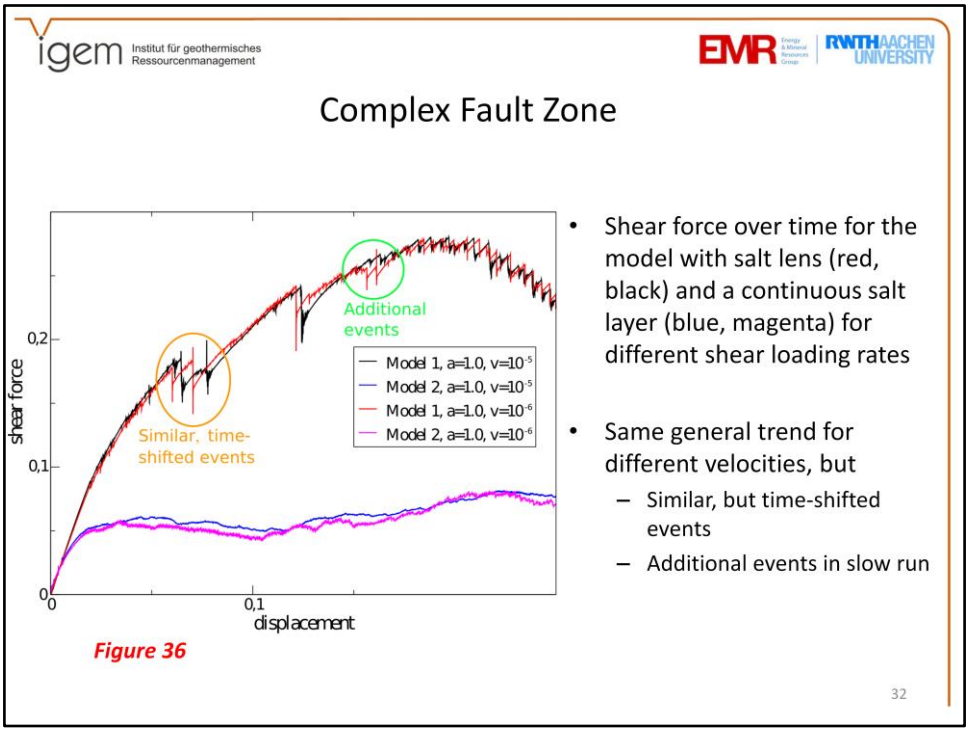

Figure 36: Shear force evolving over displacement for four simulations based on models with a salt lens (red and black curve) and with a continuous salt layer (blue and magenta curve). The two different curves for each model show the influence of slow ($v=10^{-6}$, red and magenta curve) and fast loading rate ($v=10^{-5}$, black and blue curve)

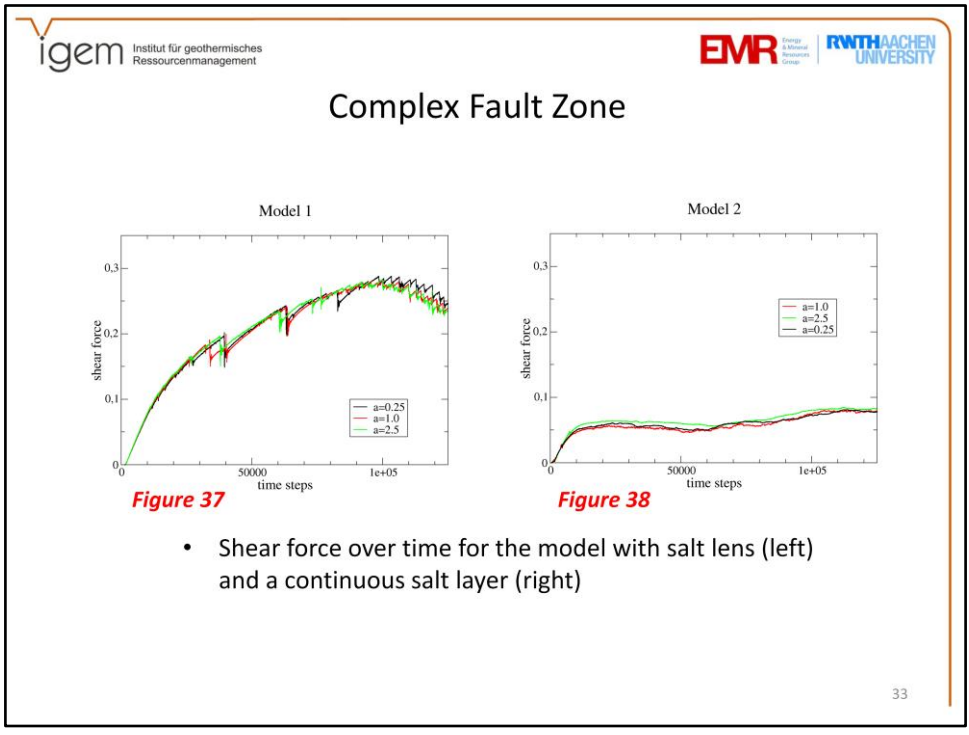

Figure 37: Shear force evolving over time for three simulations based on a model with a salt lens about half as wide as the whole model (Fig. 14) . Different colors show the effect of different viscosity parameters (black a=0.25, red a=1.0, green a=2.5)

Figure 38: Shear force evolving over time for three simulations based on a model with salt spanning the whole width of the model (Fig. 15) . Different colors show the effect of different viscosity parameters (black a=0.25, red a=1.0, green a=2.5)

Conclusions

Assuming a dilatant or hybrid behavior of faults beneath a salt layer, analog models clearly show that:

- salt flows into opening fractures and faults
- lateral flow can bring salt into extensional jogs beneath non-dilatant part of faults
- the extent to which salt will enter a fault is strongly controlled by the failure mode and fault geometry.

Using simple and complex geometries of salt analog in a fault in DEM models shows that:

- DEM can model seismicity of faults containing salt
- Salt makes fault behavior dependent on shear loading rate
- Complex interplay between stick-slip dynamics of fault and visco-elastic behavior of salt